

Positivity-preserving and entropy-bounded discontinuous Galerkin method for the chemically reacting, compressible Euler equations. Part I: The one-dimensional case

Eric J. Ching^{*}, Ryan F. Johnson, Andrew D. Kercher

Laboratories for Computational Physics and Fluid Dynamics, U.S. Naval Research Laboratory, Washington, DC, 20375, United States of America

ARTICLE INFO

Keywords:

Discontinuous Galerkin method
Combustion
Minimum entropy principle
Positivity-preserving
Entropy stability
Summation-by-parts

ABSTRACT

In this paper, we develop a fully conservative, positivity-preserving, and entropy-bounded discontinuous Galerkin scheme for simulating the multicomponent, chemically reacting, compressible Euler equations with complex thermodynamics. The proposed formulation is an extension of the fully conservative, high-order numerical method previously developed by Johnson and Kercher (2020) [14] that maintains pressure equilibrium between adjacent elements. In this first part of our two-part paper, we focus on the one-dimensional case. Our methodology is rooted in the minimum entropy principle satisfied by entropy solutions to the multicomponent, compressible Euler equations, which was proved by Gouasmi et al. (2020) [16] for nonreacting flows. We first show that the minimum entropy principle holds in the reacting case as well. Next, we introduce the ingredients, including a simple linear-scaling limiter, required for the discrete solution to have nonnegative species concentrations, positive density, positive pressure, and bounded entropy. We also discuss how to retain the aforementioned ability to preserve pressure equilibrium between elements. Operator splitting is employed to handle stiff chemical reactions. To guarantee discrete satisfaction of the minimum entropy principle in the reaction step, we develop an entropy-stable discontinuous Galerkin method based on diagonal-norm summation-by-parts operators for solving ordinary differential equations. The developed formulation is used to compute canonical one-dimensional test cases, namely thermal-bubble advection, advection of a low-density Gaussian wave, multicomponent shock-tube flow, and a moving hydrogen-oxygen detonation wave with detailed chemistry. We demonstrate that the formulation can achieve optimal high-order convergence in smooth flows. Furthermore, we find that the enforcement of an entropy bound can considerably reduce the large-scale nonlinear instabilities that emerge when only the positivity property is enforced, to an even greater extent than in the monocomponent, calorically perfect case. Finally, mass, total energy, and atomic elements are shown to be discretely conserved.

1. Introduction

The discontinuous Galerkin (DG) method [1–5] has recently gained considerable attention in the computational fluid dynamics community [6]. Several desirable properties, such as local conservation, arbitrarily high order of accuracy on unstructured grids,

^{*} Corresponding author.

E-mail address: eric.ching@nrl.navy.mil (E.J. Ching).

<https://doi.org/10.1016/j.jcp.2024.112881>

Received 23 December 2022; Received in revised form 22 December 2023; Accepted 21 February 2024

Available online 28 February 2024

0021-9991/Published by Elsevier Inc.

and suitability for heterogeneous computing systems, highlight its great potential to accurately and efficiently simulate complex fluid flows. However, it is well-known that nonlinear instabilities are easily introduced in underresolved regions and near flow-field discontinuities. This issue is exacerbated when realistic thermodynamics (e.g., the thermally perfect gas model) and multispecies chemical reactions are incorporated. For example, fully conservative schemes (not just the DG method) are known to generate spurious pressure oscillations in moving interface problems [7–9]. To remedy this issue, quasi-conservative methods are often employed, such as the double-flux scheme [10], in which the equation of state is recast based on a calorically perfect gas model using frozen, elementwise-constant auxiliary variables. The double-flux method has been utilized in a number of studies involving DG simulations of multicomponent flows [11–13]. While effective at eliminating the aforementioned pressure oscillations, the double-flux approach violates energy conservation, which can be crucial for the prediction of shock speeds and locations, as well as heat release in combustion processes. As a compromise, Lv and Ihme [12] proposed a hybrid double-flux strategy wherein a fully conservative method is employed at shocks.

On the other hand, Johnson and Kercher recently proposed an explicit, fully conservative, high-order method that can maintain pressure equilibrium (in an approximate sense) in smooth flow regions or across material interfaces when the temperature is continuous [14]. This is done via (a) exact evaluation of the thermodynamics and (b) consistent calculation of the inviscid and viscous fluxes in a special manner, which is drastically simplified through a particular choice of nodal basis. It is worth noting that their proposed strategy is not limited to DG schemes, but can be applied to other numerical methods as well. Stiff chemical reactions were handled via operator splitting. Efficient and accurate integration of the chemical source terms was achieved via an *hp*-adaptive DG method for solving ordinary differential equations, termed *DGODE*. Optimal high-order accuracy was demonstrated for smooth flows, and a suite of complex multicomponent reacting flows was computed. The high-order calculation of a three-dimensional reacting shear flow in the presence of a splitter plate did not require any additional stabilization. Also computed was a two-dimensional, moving detonation wave. Artificial viscosity was used to stabilize the shock fronts present in the solution. However, a very fine mesh was required to maintain robustness while achieving correct prediction of the cellular structures behind the shock, highlighting the difficulty of robustly and accurately simulating multidimensional detonation waves on coarse meshes, especially for high-order methods. Even if spurious pressure oscillations are sufficiently minimized, the wide range of complex flow features characterizing detonations is difficult to capture [15]. Such features include thin reaction zones, traveling pressure waves, shock-shock interactions, Kelvin-Helmholtz instabilities, vortical structures, and triple points. As previously discussed, underresolution of flow features induces instabilities that can cause solver divergence, and these instabilities may be amplified by the added nonlinearity of the variable thermodynamics, multicomponent flow, and stiff chemical reactions. Another difficulty associated with multicomponent flow is the frequent occurrence of negative species concentrations, especially since initial and boundary conditions often specify the mole fractions of certain species to be zero. Many reacting-flow solvers simply “clip” negative concentrations to zero, which violates conservation and introduces low-order errors.

In light of the above, our primary objective in this study is to develop a positivity-preserving and entropy-bounded DG scheme for simulating the multicomponent, chemically reacting Euler equations with exact thermodynamics for mixtures of thermally perfect gases. Specifically, we build upon the aforementioned fully conservative high-order method that can maintain pressure equilibrium [14]. In this first part of our two-part paper, we focus on the one-dimensional case. The unique challenges posed by realistic thermodynamics and stiff chemical source terms are discussed and addressed. *Entropy-bounded* in this context means that the specific thermodynamic entropy of the discrete solution is bounded from below, an idea rooted in the minimum entropy principle satisfied by entropy solutions to the compressible, multicomponent Euler equations. This principle was recently proved for the nonreacting case by Gouasmi et al. [16], which is an important prerequisite of this work. The developed formulation in general preserves order of accuracy for smooth solutions. Our main contributions are as follows:

- A minimum entropy principle for the compressible, multicomponent, chemically reacting Euler equations is demonstrated, which follows naturally from the proof in [16].
- In a DG framework, we extend the fully conservative high-order discretization in [14] to be positivity-preserving and entropy-bounded. We also discuss a different local entropy bound that is less restrictive than that previously introduced in [17] in the context of the monocomponent Euler equations.
- To provably guarantee satisfaction of the minimum entropy principle in the temporal integration of stiff chemical source terms, we extend *DGODE* by developing an entropy-stable *DGODE* based on diagonal-norm summation-by-parts (SBP) operators. This involves deriving a new entropy-conservative two-point numerical state function (note that similar entropy-conservative numerical state functions were derived for the monocomponent Euler, shallow-water, and ideal magnetohydrodynamics equations by Friedrich et al. [18] in the context of an entropy-stable space-time DG discretization).
- We employ the proposed entropy-bounded DG method to robustly and accurately compute a series of canonical one-dimensional test cases. Mass, energy, and atom conservation are maintained. The proposed formulation more effectively suppresses spurious oscillations than the positivity-preserving DG scheme (i.e., an equivalent scheme but without the entropy bound enforced). In particular, we find that the relative benefit of enforcing an entropy bound is significantly greater in the multicomponent, thermally perfect setting than in monocomponent, calorically perfect setting.

In Part II [19], we extend the entropy-bounded DG scheme to multiple dimensions on arbitrary elements. Our multidimensional extension is a further generalization of the multidimensional positivity-preserving/entropy-bounded schemes currently in the literature [20,21,17,22]. Specifically, restrictions on the numerical flux, physical modeling, element shape, polynomial order of the geometric approximation, and/or quadrature rules are relaxed. Complex detonation waves in two and three dimensions are com-

puted. We find that whereas the positivity-preserving DG scheme is often not sufficiently stable (even with artificial viscosity to stabilize strong discontinuities), enforcing an entropy bound enables robust calculations on relatively coarse meshes.

1.1. Background

Various stabilization strategies for high-order DG schemes have been introduced in the literature. Artificial viscosity is a popular approach that very effectively suppresses oscillations and is perfectly compatible with high polynomial orders, arbitrary elements, and general equation sets [23–25]. However, there are certain limitations that discourage an overreliance on artificial viscosity for suppressing *all* instabilities. First, it can significantly pollute accuracy, especially in smooth regions of the flow. As such, it should ideally be added only where necessary (e.g., strong shocks that are otherwise difficult to robustly capture). Second, design of a shock sensor that can reliably detect discontinuous flow features for general configurations remains an open problem. Even in a single flow configuration that involves discontinuities of varying strengths (as is the case for detonations), it is difficult to detect all such discontinuities and add the “right” amount of artificial viscosity. Third, there is typically a very strong dependence on tunable parameters.

A common alternative to artificial viscosity is limiting. WENO-type [26,27], TVD/TVB [28,29], and moment limiters [30] are well-known examples. However, it can be difficult to extend these limiters to arbitrary polynomial orders for both the solution and geometric approximations, as well as to general equation sets. Furthermore, these limiters are not guaranteed to yield physically admissible solutions (i.e., positive density and pressure), a drawback of artificial viscosity as well. An alternative approach for maintaining robustness is to align the grid with discontinuities. Recent formulations that do so in an implicit manner by treating the grid as a variable were developed by Corrigan et al. [31] and Zahr and Persson [32]. An encouraging preliminary effort to apply implicit shock tracking to reacting flow is discussed in [33], in which supersonic inviscid reacting flow over a two-dimensional wedge with simple thermodynamics and chemistry was computed.

Recently, positivity-preserving DG schemes [20,34,21,35] have seen considerable success in solving the monocomponent, non-reacting Euler equations with explicit time stepping. These schemes prevent the occurrence of negative densities and pressures under a constraint on the time step size, a positivity-preserving numerical flux, and a limiting procedure consisting of a simple linear “squeezing” of the solution towards its cell average. The limiting operator is conservative and maintains order of accuracy for smooth solutions. However, the limiter is not very effective at dampening oscillations. The positivity-preserving DG method was extended to the entropy-bounded DG scheme by Zhang and Shu [36], in which an additional limiting step based on a Newton search was introduced to enforce a global entropy bound. Note that it is implicitly assumed that an entropy-bounded scheme is also positivity-preserving. Under their invariant-region-preserving DG framework, Jiang and Liu [22] introduced a more straightforward limiter to enforce the entropy principle in an algebraic manner, which is particularly desirable in the multicomponent, thermally perfect case due to the cost of evaluating complex thermodynamics. Lv and Ihme [17] further extended the entropy-bounded DG scheme (for the monocomponent Euler equations) by relaxing restrictions on the geometry and quadrature rules. They also introduced a local entropy bound. Numerical tests demonstrated the superiority of the entropy-bounded DG scheme for suppressing spurious oscillations, compared to the positivity-preserving DG method. Lv and Ihme later applied entropy bounding to their reacting flow DG solver [37], which utilizes the double-flux approach discussed above. The frozen thermodynamics and relaxation towards a calorically perfect gas model circumvent the difficulties of extending the entropy-bounded DG method to reacting flow with exact thermodynamics and non-calorically-perfect gases. Furthermore, the physico-mathematical validity of combining the double-flux model with enforcement of a discrete minimum entropy principle is not immediately clear. We also note that these positivity-preserving and entropy-bounded DG methods are related to the recent geometric quasilinearization framework by Wu and Shu [38], as well as the invariant-domain-preserving schemes based on graph viscosity by, for example, Guermond et al. [39] and Pazner [40], which employ a convex limiting procedure relying on an iterative line search.

Before concluding this section, we note several other efforts to compute chemically reacting flows with DG schemes in a stable manner. Gutierrez-Jorquera and Kummer [41] computed steady-state diffusion flames using a low-Mach pressure-based solver and a one-step reaction mechanism. May et al. [42] simulated steady hypersonic flows with some high-enthalpy effects using a hybridized DG solver that employs artificial viscosity for shock capturing. Papoutsakis et al. [43] computed chemically reacting hypersonic flow over a double cone with a TVB limiter; however, only a linear polynomial approximation of the solution was employed, and there were discrepancies with finite-volume and experimental results. A number of positivity-preserving DG schemes for the reacting Euler equations have also been developed. For example, Zhang and Shu [34] and Wang et al. [44] extended the positivity-preserving DG scheme to handle source terms with explicit time stepping. Complex thermodynamics and stiff source terms were not addressed. Du and Yang [45] and Du et al. [46] presented a positivity-preserving DG method based on a new explicit, exponential Runge-Kutta (RK)/multistep time integration scheme that can handle stiff source terms [47]. However, the temporal order of accuracy is strongly dependent on the initial conditions. Other positivity-preserving time integrators compatible with stiff source terms include implicit Patankar-type RK schemes [48–50], which have been applied to finite difference [48,49] and finite volume [50] discretizations of the reacting Euler equations. These schemes are still undergoing development, and there may be issues with extending them to DG discretizations [48]. An additional obstacle of both exponential RK/multistep and Patankar-type RK schemes is proper enforcement of the minimum entropy principle. For these reasons and due to its proven past success, we elect to still employ operator splitting to deal with stiff source terms. Nevertheless, exponential RK/multistep and Pantankar-type schemes are indeed worthy of future consideration.

That we use an entropy-stable DG discretization to temporally integrate the chemical source terms may cause readers to question why an entropy-stable DG discretization is not also employed for the transport step. Note that entropy-stable schemes guarantee

the global integral of mathematical entropy to be nonincreasing in time (assuming periodic or entropy-stable boundary conditions), whereas entropy-bounded schemes enforce, in a pointwise fashion, the specific thermodynamic entropy to be greater than some lower bound. Entropy-stable DG schemes for multicomponent (nonreacting) flows have emerged only recently [51,52]. For general hyperbolic conservation laws, there are various ways to achieve entropy stability; two of the most well-known are as follows: (a) the entropy variables, instead of the conservative variables, are directly solved for, and (b) SBP operators are used to approximate discrete derivatives. The first approach, in which the conservative variables depend implicitly on the polynomial approximation of the entropy variables, is not appropriate for explicit time stepping, which we employ in this work (for the transport terms). Furthermore, with the typical choice of entropy, the entropy variables are undefined when any of the partial densities vanishes [51]. Conversely, the second approach, which has surged in popularity in recent years, is compatible with explicit time stepping (although small amounts of mathematical entropy can still be destroyed as a result of the time integration scheme) and does not assume exact integration to provably guarantee entropy stability. Belonging to this category are the methods by Renac [52] and Peyvan et al. [53]. On unstructured grids, particularly those with (possibly curved) simplicial elements, current SBP-based entropy-stable methods can become suboptimal [54], require direct use of the entropy variables (even if the conservative variables are the unknowns) [55,56], and/or significantly increase in complexity [55,57,56,58]. Note that these issues are not present in the developed entropy-stable DGODE (except a moderate increase in complexity), which entails a one-dimensional discretization in time. Due to the above factors, as well as the relative simplicity of the entropy-bounded DG scheme and its compatibility with the pressure-equilibrium-maintaining discretization by Johnson and Kercher [14], we choose to employ the proposed entropy-bounded method for the transport step. Nevertheless, we emphasize that we are not ruling out entropy-stable schemes; advancements to these formulations are rapid and their potential is evident [59]. Finally, it should be noted that although the construction of entropy-stable and entropy-bounded methods rely on different techniques, entropy stability and entropy boundedness are not necessarily mutually exclusive. Depending on the type of entropy-stable scheme, it should, in principle, be feasible to achieve discrete satisfaction of both properties.

The remainder of this paper is organized as follows. Sections 2 and 3 summarize the governing equations and basic DG discretization, respectively. Section 4 reviews the minimum entropy principle associated with the compressible, multicomponent, nonreacting Euler equations and extends it to the reacting Euler equations. The next section presents the positivity-preserving and entropy-bounded DG formulation for the transport step. We then discuss the entropy-stable DG discretization for the reaction step in Section 6. Results for fundamental nonreacting test cases and one-dimensional detonation-wave simulations are given in the following section. We close the paper with concluding remarks.

2. Governing equations

The compressible, multicomponent, chemically reacting Euler equations are given as

$$\frac{\partial y}{\partial t} + \nabla \cdot \mathcal{F}(y) - S(y) = 0 \quad (2.1)$$

where $t \in \mathbb{R}^+$ is time, $y(x, t) : \mathbb{R}^d \times \mathbb{R}^+ \rightarrow \mathbb{R}^m$ is the conservative state vector (with $x = (x_1, \dots, x_d)$ denoting the physical coordinates), $\mathcal{F}(y) : \mathbb{R}^m \rightarrow \mathbb{R}^{m \times d}$ is the convective flux, $S(y) : \mathbb{R}^m \rightarrow \mathbb{R}^m$ is the chemical source term. The state vector is expanded as

$$y = \left(\rho v_1, \dots, \rho v_d, \rho e_t, C_1, \dots, C_{n_s} \right)^T, \quad (2.2)$$

where n_s is the number of species (which yields $m = d + n_s + 1$), ρ is density, $v = (v_1, \dots, v_d)$ is the velocity, e_t is the mass-specific total energy, and $C = (C_1, \dots, C_{n_s})$ are the species concentrations. The density is computed from the species concentrations as

$$\rho = \sum_{i=1}^{n_s} \rho_i = \sum_{i=1}^{n_s} W_i C_i,$$

where ρ_i is the partial density and W_i is the molecular mass of the i th species. The mass fraction of the i th species is defined as

$$Y_i = \frac{\rho_i}{\rho}.$$

The k th spatial convective flux component is written as

$$\mathcal{F}_k(y) = \left(\rho v_k v_1 + P \delta_{k1}, \dots, \rho v_k v_d + P \delta_{kd}, v_k (\rho e_t + P), v_k C_1, \dots, v_k C_{n_s} \right)^T, \quad (2.3)$$

where P is the pressure. The mass-specific total energy is the sum of the specific internal and kinetic energies, given by

$$e_t = u + \frac{1}{2} \sum_{k=1}^d v_k v_k,$$

where the (mixture-averaged) mass-specific internal energy, u , is the mass-weighted sum of the mass-specific internal energies of each species:

$$u = \sum_{i=1}^{n_s} Y_i u_i.$$

This work assumes thermally perfect gases, with u_i given by [60]

$$u_i = h_i - R_i T = h_{\text{ref},i} + \int_{T_{\text{ref}}}^T c_{p,i}(\tau) d\tau - R_i T,$$

where h_i is the mass-specific enthalpy of the i th species, $R_i = R^0/W_i$ (with $R^0 = 8314.4621 \text{ J K mol}^{-1} \text{ K}^{-1}$ denoting the universal gas constant), T is the temperature, T_{ref} is the reference temperature (298.15 K), $h_{\text{ref},i}$ is the reference-state species formation enthalpy, and $c_{p,i}$ is the mass-specific heat capacity at constant pressure of the i th species. $c_{p,i}$ is computed from an n_p -order polynomial as

$$c_{p,i} = \sum_{k=0}^{n_p} a_{ik} T^k, \quad (2.4)$$

based on the NASA coefficients [61,62]. The mass-specific thermodynamic entropy of the mixture is defined as

$$s = \sum_{i=1}^{n_s} Y_i s_i,$$

with s_i given by

$$s_i = s_i^o - R_i \log \frac{P_i}{P_{\text{ref}}}, \quad s_i^o = s_{\text{ref},i}^o + \int_{T_{\text{ref}}}^T \frac{c_{p,i}(\tau)}{\tau} d\tau, \quad (2.5)$$

where $s_{\text{ref},i}^o$ is the species formation entropy at the reference temperature and reference pressure ($P_{\text{ref}} = 1 \text{ atm}$), s_i^o denotes the species entropy at atmospheric pressure, and $P_i = C_i R^0 T$ is the partial pressure. s_i can also be expressed as [60,16,51]

$$s_i = s_{\text{ref},i}^o + \int_{T_{\text{ref}}}^T \frac{c_{v,i}(\tau)}{\tau} d\tau - R_i \log \frac{C_i}{C_{\text{ref}}},$$

where $C_{\text{ref}} = P_{\text{ref}}/R^0 T_{\text{ref}}$ is the reference concentration and $c_{v,i} = c_{p,i} - R_i$ is the mass-specific heat capacity at constant volume of the i th species. Summing up the partial pressures yields the equation of state for the mixture:

$$P = R^0 T \sum_{i=1}^{n_s} C_i. \quad (2.6)$$

u_i , h_i , and s_i^o are computed by integrating Equation (2.4). For example, u_i is calculated as

$$u_i = b_{i0} + \sum_{k=0}^{n_p} \frac{a_{ik}}{k+1} T^{k+1} - R_i T = \sum_{k=0}^{n_p+1} b_{ik} T^k, \quad (2.7)$$

where b_{i0} is the integration constant and

$$b_{ik} = \begin{cases} \frac{a_{i,k-1}}{k}, & k > 1 \\ a_{i0} - R_i, & k = 1. \end{cases}$$

2.1. Chemical reaction rates

The source term in Equation (2.1) is a smooth function of the state variables, written as [63]

$$S(y) = (0, \dots, 0, \omega_1, \dots, \omega_{n_s})^T, \quad (2.8)$$

where ω_i is the production rate of the i th species, which satisfies mass conservation:

$$\sum_{i=1}^{n_s} W_i \omega_i = 0. \quad (2.9)$$

The production rate is computed as

$$\omega_i = \sum_{j=1}^{n_r} \nu_{ij} q_j.$$

n_r is the number of reactions, $v_{ij} = v_{ij}^r - v_{ij}^f$ is the difference between the reverse (v_{ij}^r) and the forward stoichiometric coefficients (v_{ij}^f), and q_j is the rate of progress of the j th reaction, computed as

$$q_j = k_j^f \prod_{i=1}^{n_s} C_i^{v_{ij}^f} - k_j^r \prod_{i=1}^{n_s} C_i^{v_{ij}^r}, \quad (2.10)$$

where k_j^f and k_j^r are the forward and reverse rate constants, respectively, of the j th reaction. The forward and reverse rate constants are related via the equilibrium constant,

$$K_j^e = \exp\left(-\frac{\Delta G_j'}{R^0 T}\right) \left(\frac{P_{\text{ref}}}{R^0 T}\right)^{\sum_i v_{ij}}, \quad (2.11)$$

where $\Delta G_j'$ is the change in reference-state Gibbs free energy for the j th reaction, given as

$$\Delta G_j' = \sum_{i=1}^{n_s} v_{ij} W_i h_i - T \sum_{i=1}^{n_s} v_{ij} W_i s_i'.$$

Introducing the reduced chemical potentials of the i th species,

$$\begin{aligned} \mu_i &= \frac{g_i}{R^0 T}, \\ \mu_i^u &= \mu_i - \frac{1}{W_i} \log C_i, \end{aligned}$$

where $g_i = h_i - T s_i$ is the Gibbs function of the i th species, the equilibrium constant can also be written as [60, Chapter 6.4]

$$K_j^e = \exp\left(-\sum_{i=1}^{n_s} v_{ij} W_i \mu_i^u\right). \quad (2.12)$$

There exist various models for approximating the forward rate constants in Equation (2.10), several of which will be briefly discussed next.

2.1.1. Arrhenius reactions

The Arrhenius form is the most common model for approximating reaction rates. The forward rate constants are computed as

$$k_j^f = A_j T^{b_j} \exp\left(-\frac{E_j}{R^0 T}\right),$$

where $A_j > 0$ and b_j are parameters and $E_j \geq 0$ is the activation energy [60,63].

2.1.2. Three-body reactions

These reactions require a “third body” in order to proceed. Dissociation and recombination reactions are often of this type. The rate of progress is scaled by a prefactor as [63]

$$q_j = \left(\sum_{i=1}^{n_s} \alpha_{ij} C_i\right) \left(k_j^f \prod_{i=1}^{n_s} C_i^{v_{ij}^f} - k_j^r \prod_{i=1}^{n_s} C_i^{v_{ij}^r}\right),$$

where α_{ij} are the third-body efficiencies.

2.1.3. Unimolecular/recombination fall-off reactions

Unimolecular/recombination fall-off reactions incorporate a dependence on pressure. In general, this model predicts an increase in the reaction rate with increasing pressure. For brevity, we drop the j subscript and f superscript. Given Arrhenius-type low-pressure and high-pressure limits for the rate constant (k_0 and k_∞ , respectively), k is computed as

$$k = k_\infty \left(\frac{P_r}{1 + P_r}\right) F, \quad (2.13)$$

where P_r is the reduced pressure, defined as

$$P_r = \frac{k_0}{k_\infty} \sum_{i=1}^{n_s} \alpha_i C_i.$$

There are different ways to compute F in Equation (2.13). With the Lindemann [64] approach, F is simply unity. In the Troe [65] form, F is given by

$$\log F = \frac{\log F_{\text{cent}}}{1 + \left[\frac{\log P_r + c_1}{c_2 - c_3 (\log P_r + c_1)} \right]^2},$$

where the definitions of c_1 , c_2 , c_3 , and F_{cent} are given in [65].

2.1.4. Chemically activated bimolecular reactions

Reactions of this type are also pressure-dependent, but the reaction rates typically decrease with increasing pressure. The rate constants are computed as [63]

$$k = k_0 \left(\frac{1}{1 + P_r} \right) F,$$

where k_0 , P_r , and F are calculated as in Section 2.1.3.

3. Discontinuous Galerkin discretization

In this section, we briefly describe the DG discretization of the governing equations and review the techniques proposed in [14] to prevent spurious pressure oscillations in smooth regions of the flow.

Let $\Omega \subset \mathbb{R}^d$ be the d -dimensional computational domain (with boundary $\partial\Omega$) partitioned by \mathcal{T} , which consists of non-overlapping cells κ with boundaries $\partial\kappa$. Let \mathcal{E} denote the set of interfaces ϵ , with $\cup_{\epsilon \in \mathcal{E}} \epsilon = \cup_{\kappa \in \mathcal{T}} \partial\kappa$. \mathcal{E} consists of the interior interfaces,

$$\epsilon_I \in \mathcal{E}_I = \{ \epsilon_I \in \mathcal{E} \mid \epsilon_I \cap \partial\Omega = \emptyset \},$$

and boundary interfaces,

$$\epsilon_\partial \in \mathcal{E}_\partial = \{ \epsilon_\partial \in \mathcal{E} \mid \epsilon_\partial \subset \partial\Omega \},$$

such that $\mathcal{E} = \mathcal{E}_I \cup \mathcal{E}_\partial$. At interior interfaces, there exists $\kappa^+, \kappa^- \in \mathcal{T}$ such that $\epsilon_I = \partial\kappa^+ \cap \partial\kappa^-$. n^+ and n^- denote the outward facing normal of κ^+ and κ^- , respectively, with $n^+ = -n^-$. The discrete (finite-dimensional) subspace V_h^p over \mathcal{T} is defined as

$$V_h^p = \left\{ \mathbf{v} \in [L^2(\Omega)]^m \mid \forall \kappa \in \mathcal{T}, \mathbf{v}|_\kappa \in [\mathcal{P}_p(\kappa)]^m \right\}, \quad (3.1)$$

where, for $d = 1$, $\mathcal{P}_p(\kappa)$ is the space of polynomial functions of degree no greater than p in κ . For $d > 1$, the choice of polynomial space typically depends on the element type [66].

The semi-discrete form of the governing equations (Equation (2.1)) is given as: find $y \in V_h^p$ such that

$$\sum_{\kappa \in \mathcal{T}} \left(\frac{\partial y}{\partial t}, \mathbf{v} \right)_\kappa - \sum_{\kappa \in \mathcal{T}} (F(y), \nabla \mathbf{v})_\kappa + \sum_{\epsilon \in \mathcal{E}} (F^\dagger(y^+, y^-, n^+), [\![\mathbf{v}]\!])_\epsilon - \sum_{\kappa \in \mathcal{T}} (S(y), \mathbf{v})_\kappa = 0 \quad \forall \mathbf{v} \in V_h^p, \quad (3.2)$$

where (\cdot, \cdot) denotes the inner product, $F^\dagger(y^+, y^-, n^+)$ is the numerical flux, and $[\![\cdot]\!]$ is the jump operator, given by $[\![\mathbf{v}]\!] = \mathbf{v}^+ - \mathbf{v}^-$ at interior interfaces and $[\![\mathbf{v}]\!] = \mathbf{v}^+$ at boundary interfaces. Applying a standard, fully explicit time stepping scheme to Equation (3.2) would yield an exceedingly small time step due to the stiff chemical source terms. As such, operator splitting is employed to decouple the temporal integration of the convection operator from that of the source term. Specifically, we apply Strang splitting [67] over a given interval $(t_0, t_0 + \Delta t]$ as

$$\frac{\partial y}{\partial t} + \nabla \cdot F(y) = 0 \text{ in } \Omega \times (t_0, t_0 + \Delta t/2], \quad (3.3)$$

$$\frac{\partial y}{\partial t} - S(y) = 0 \text{ in } (t_0, t_0 + \Delta t], \quad (3.4)$$

$$\frac{\partial y}{\partial t} + \nabla \cdot F(y) = 0 \text{ in } \Omega \times (t_0 + \Delta t/2, t_0 + \Delta t], \quad (3.5)$$

where Equations (3.3) and (3.5) are integrated in time with an explicit RK-type scheme, while Equation (3.4) is solved using a fully implicit, temporal DG discretization for ODEs (DGODE). Details on DGODE and its extension to entropy-stable DGODE are given in Section 6. The solution of (3.3) at $t = t_0 + \Delta t/2$ is the initial condition of (3.4), and the solution of (3.4) at time $t = t_0 + \Delta t$ is the initial condition of (3.5). Strang splitting is a popular splitting method that has been employed in many reacting-flow simulations [68–73]. It is second-order accurate and strongly stable [67]. The time-step size, Δt , is thus restricted by constraints associated with the transport step, which will be discussed later in this paper. More sophisticated operator-splitting schemes can be employed as well. For example, simpler balanced splitting [74] is similarly strongly stable and second-order accurate; however, unlike Strang splitting, it is also steady-state-preserving, which can be important for dynamic systems near bifurcation, while maintaining comparable computational cost. Note that higher-order splitting is possible only by permitting backward-in-time substeps or substeps that go forward in complex time [75].

Unless otherwise specified, the volume and surface terms in Equation (3.2) are evaluated using a quadrature-free approach [76, 77]. Throughout this work, we employ a nodal basis, such that the element-local polynomial approximation of the solution is expanded as

$$y_\kappa = \sum_{j=1}^{n_b} y_\kappa(x_j) \phi_j, \quad (3.6)$$

where n_b is the number of basis functions, $\{\phi_1, \dots, \phi_{n_b}\}$ are the basis functions, and $\{x_1, \dots, x_{n_b}\}$ are the node coordinates. Its average over κ is given by

$$\bar{y}_\kappa = \frac{1}{|\kappa|} \int_\kappa y dx, \quad (3.7)$$

where $|\kappa|$ is the volume of κ . In the evaluation of the second and third integrals in Equation (3.2), the nonlinear convective flux can be approximated as

$$F_\kappa \approx \sum_{k=1}^{n_c} F(y_\kappa(x_k)) \varphi_k, \quad (3.8)$$

where $n_c \geq n_b$ and $\{\varphi_1, \dots, \varphi_{n_c}\}$ is a set of (potentially different) polynomial basis functions. If $n_c = n_b$ and the integration points are included in the set of solution nodes (e.g., Gauss-Lobatto points for tensor-product elements), then pressure equilibrium is well-maintained (in an approximate sense) [14]. However, over-integration (i.e., $n_c > n_b$) is often necessary to minimize aliasing errors and improve stability. Unfortunately, standard over-integration, as defined in Equation (3.8), causes a loss of pressure equilibrium and generation of spurious pressure oscillations at material interfaces [14]. Instead, Johnson and Kercher [14] proposed the following approximation of the convective flux:

$$F_\kappa \approx \sum_{k=1}^{n_c} F(\tilde{y}_\kappa(x_k)) \varphi_k, \quad (3.9)$$

where $\tilde{y}: \mathbb{R}^m \times \mathbb{R} \rightarrow \mathbb{R}^m$ is a modified state defined as

$$\tilde{y}(y, \tilde{P}) = \left(\rho v_1, \dots, \rho v_d, \tilde{\rho} u(C_1, \dots, C_{n_s}, \tilde{P}) + \frac{1}{2} \sum_{k=1}^d \rho v_k v_k, C_1, \dots, C_{n_s} \right)^T. \quad (3.10)$$

\tilde{P} is a polynomial approximation of the pressure that interpolates onto the span of $\{\phi_1, \dots, \phi_{n_b}\}$ as

$$\tilde{P}_\kappa = \sum_{j=1}^{n_b} P(y_\kappa(x_j)) \phi_j,$$

and the modified internal energy, $\tilde{\rho} u$, is evaluated from the modified pressure and unmodified species concentrations. Interpolating the convective flux (including the numerical flux function) in this manner achieves approximate pressure equilibrium both internally and between adjacent elements. Of course, with finite resolution, slight deviations from pressure equilibrium are inevitable; nevertheless, apart from severely underresolved computations, these deviations generally remain small and do not generate large-scale pressure oscillations that cause the solver to crash, which is not the case if standard flux interpolation (3.8) is employed. Additional information on the basic DG discretization, enforcement of boundary conditions, and nonlinear flux interpolation, as well as a detailed discussion of the conditions under which pressure oscillations are generated, can be found in [14].

4. Minimum entropy principle

It is well-known that in the presence of discontinuities, weak solutions to general systems of hyperbolic conservation laws, including the multicomponent Euler equations, are not unique [78]. As such, physical solutions are typically identified as those that satisfy entropy conditions, written as (in the absence of source terms)

$$\frac{\partial U}{\partial t} + \nabla \cdot F^s \leq 0, \quad (4.1)$$

where $U(y): \mathbb{R}^m \rightarrow \mathbb{R}$ is a given convex (mathematical) entropy function and $F^s(y): \mathbb{R}^m \rightarrow \mathbb{R}^d$ is the corresponding spatial entropy flux satisfying

$$v^T \frac{\partial F}{\partial y} = \frac{\partial F^s}{\partial y},$$

with v , the entropy variables, defined as

$$v = \left(\frac{\partial U}{\partial y} \right)^T.$$

The mapping from the conservative variables to the entropy variables is one-to-one and symmetrizes the system [79]. *Entropy solutions* are weak solutions that satisfy (4.1) for all entropy/entropy-flux pairs. We also introduce the entropy potential and the corresponding entropy flux potential:

$$(U, F^p) = (v^T y - U, v^T F - F^s), \quad (4.2)$$

which will be used in Section 6. For the multicomponent Euler equations, $U = -\rho s$ and $F^s = -\rho s v$ form a common admissible entropy/entropy-flux pair [16,60], assuming $C_i > 0$ and $T > 0$. Note the distinction between the mathematical entropy and the thermodynamic entropy (per unit volume); they are typically of opposite sign.

4.1. Review: minimum entropy principle in the compressible, multicomponent, nonreacting Euler equations

Gouasmi et al. [16] recently proved a minimum entropy principle satisfied by entropy solutions to the multicomponent, nonreacting Euler equations, which means that the spatial minimum of the specific thermodynamic entropy is a nondecreasing function of time. In this subsection, we summarize the main steps of the proof, which itself builds on the proof by Tadmor [80] of a minimum entropy principle in the monocomponent Euler equations.

Tadmor [81] showed that by integrating (4.1) over the truncated cone $C = \{|x| \leq R + v_{\max}(t - \tau) | 0 \leq \tau \leq t\}$ yields the following local inequality:

$$\int_{|x| \leq R} U(y(x, t)) dx \leq \int_{|x| \leq R + v_{\max} t} U(y(x, 0)) dx, \quad (4.3)$$

where v_{\max} is the maximum speed in the domain at $t = 0$. If we consider entropy/entropy-flux pairs of the form

$$(U, F^s) = (-\rho f(s), -\rho v f(s)), \quad (4.4)$$

where f is a smooth function of s , (4.3) then becomes

$$\int_{|x| \leq R} \rho(x, t) \cdot f(s(y(x, t))) dx \geq \int_{|x| \leq R + v_{\max} t} \rho(x, 0) \cdot f(s(y(x, 0))) dx. \quad (4.5)$$

Consider the following choice for $f(s)$:

$$f_0(s) = \min\{s - s_0, 0\},$$

where s_0 is the essential infimum of the specific thermodynamic entropy in the subdomain $\Omega_R = \{|x| \leq R + v_{\max} t\}$,

$$s_0 = \text{Ess inf}_{|x| \leq R + v_{\max} t} s(x, 0).$$

Although $f_0(s)$ is not a smooth function of s , it can be written as the limit of a sequence of smooth functions, $f_0(s) = \lim_{\epsilon \rightarrow 0} f_\epsilon(s)$, where $f_\epsilon(s)$ is defined as [16]

$$f_\epsilon(s) = \int_{-\infty}^{\infty} f_0(s - \mathfrak{s}) g_\epsilon(\mathfrak{s}) d\mathfrak{s},$$

with

$$g_\epsilon(\mathfrak{s}) = \frac{1}{\epsilon} \frac{\exp\left(-\frac{\mathfrak{s}^2}{\epsilon^2}\right)}{\sqrt{\pi}}, \quad \epsilon > 0.$$

The first and second derivatives of $f_\epsilon(s)$ satisfy the following conditions:

$$\frac{df_\epsilon}{ds} > 0, \quad \frac{d^2 f_\epsilon}{ds^2} < 0.$$

Gouasmi et al. [16] proved the key result that the entropy/entropy-flux pairs $(U, F^s) = (-\rho f_\epsilon(s), -\rho v f_\epsilon(s))$, with $\epsilon > 0$, are admissible. In particular, they showed that a conservation equation (for smooth solutions) for said pairs can be obtained and that the entropy functions are convex with respect to the conservative variables.

With $U = -\rho f_0(s)$, it can be shown that the inequality (4.5) yields, for $|x| \leq R$,

$$s(x, t) \geq s_0 = \text{Ess inf}_{|x| \leq R + v_{\max} t} s(x, 0), \quad (4.6)$$

which is the minimum entropy principle for the compressible, multicomponent Euler equations. Note that only the entropy inequalities associated with $U = -\rho f_\epsilon(s)$ need to be satisfied for a minimum entropy principle to hold.

4.2. Minimum entropy principle in the compressible, multicomponent, reacting Euler equations

We now extend the result in the previous subsection to the reacting Euler equations, where the only difference is the inclusion of the chemical source terms (Equation (2.8)). The presence of the chemical source terms, which are smooth functions of only the state variables, modifies the entropy inequality (4.1) satisfied by entropy solutions as [82–84]

$$\frac{\partial U}{\partial t} + \nabla \cdot \mathcal{F}^S \leq v^T S, \quad (4.7)$$

where the RHS represents the mathematical entropy production rate due to the source term. If $v^T S \leq 0$ (i.e., the entropy production is nonpositive), the entropy inequality in (4.1) for the homogeneous system is recovered. The local inequality in (4.3) can then be obtained by again integrating over $C = \{|x| \leq R + v_{\max}(t - \tau) | 0 \leq \tau \leq t\}$. If, in particular, $v^T S \leq 0$ for entropy functions of the form $U = -\rho f_\epsilon(s)$, $\forall \epsilon > 0$, the remaining arguments in Section 4.1 can be used to establish the same minimum entropy principle in Equation (4.6) for the reacting Euler equations. As such, we focus on showing $v^T S \leq 0$ with $U = -\rho f_\epsilon(s)$, $\forall \epsilon > 0$.

Consider again entropy/entropy-flux pairs of the form $(U, \mathcal{F}^S) = (-\rho f(s), -\rho v f(s))$. The corresponding entropy variables are given as

$$v = \begin{pmatrix} \frac{df}{ds} \frac{v_1}{T} \\ \vdots \\ \frac{df}{ds} \frac{v_d}{T} \\ -\frac{df}{ds} \frac{T_1}{T} \\ \vdots \\ W_1 \frac{df}{ds} \left(\frac{g_1 - \frac{1}{2} \sum_{k=1}^d v_k v_k}{T} + s \right) - W_1 f \\ \vdots \\ W_{n_s} \frac{df}{ds} \left(\frac{g_{n_s} - \frac{1}{2} \sum_{k=1}^d v_k v_k}{T} + s \right) - W_{n_s} f \end{pmatrix},$$

which differ slightly from the entropy variables derived by Gouasmi et al. [16] since they used partial densities instead of species concentrations in the vector of state variables. The entropy production rate due to chemical reactions, $v^T S$, is then written as

$$\begin{aligned} v^T S &= \sum_{i=1}^{n_s} \left[W_i \frac{df}{ds} \left(\frac{g_i - \frac{1}{2} \sum_{k=1}^d v_k v_k}{T} + s \right) - W_i f \right] \omega_i \\ &= \frac{df}{ds} \sum_{i=1}^{n_s} W_i \omega_i \frac{g_i}{T} + \left(-\frac{1}{2} \frac{\sum_{k=1}^d v_k v_k}{T} \frac{df}{ds} + s \frac{df}{ds} - f \right) \sum_{i=1}^{n_s} W_i \omega_i \\ &= \frac{df}{ds} \sum_{i=1}^{n_s} W_i \omega_i \frac{g_i}{T}, \end{aligned}$$

where the last equality is due to mass conservation, as given by Equation (2.9). Since $\frac{df_\epsilon}{ds} > 0$, $\forall \epsilon > 0$, a minimum entropy principle holds under the condition

$$\sum_{i=1}^{n_s} W_i \omega_i \frac{g_i}{T} \leq 0. \quad (4.8)$$

The term on the LHS, $\sum_{i=1}^{n_s} W_i \omega_i g_i / T$, is precisely the entropy production rate for $U = -\rho s$, which Giovangigli [60, Chapter 6.4] already showed to be nonpositive. Note that this is equivalent to a nonnegative production rate of *thermodynamic* entropy per unit volume. A minimum entropy principle in the compressible, multicomponent, reacting Euler equations thus holds. Another consequence of (4.8) is that the entropy production rate for any entropy function of the form $U = -\rho f(s)$ is nonpositive provided that $\frac{df}{ds} \geq 0$.

5. Transport step: entropy-bounded discontinuous Galerkin scheme in one dimension

In this section, we detail the entropy-bounded DG methodology for solving Equations (3.3) and (3.5) (i.e., the explicit time integrations without source terms in the operator splitting strategy) while accounting for the modified flux interpolation in Equation (3.9). We build on related entropy-bounded DG schemes for the monocomponent Euler equations [36,17,22]. These schemes are formulated as extensions of positivity-preserving DG methods [20,34,35] since the thermodynamic entropy is well-defined only for positive densities and pressures and enforcement of an entropy constraint can be straightforwardly incorporated into the positivity-preserving framework. The one-dimensional entropy-bounded DG scheme is presented in Section 5.2, then extended to multiple dimensions in Part II [19].

5.1. Preliminaries

Let \mathcal{G}_σ denote the following set:

$$\mathcal{G}_\sigma = \left\{ y \mid C_1 > 0, \dots, C_{n_s} > 0, \rho u^* > 0, s \geq \sigma \right\}, \quad (5.1)$$

where $\sigma \in \mathbb{R}$ and u^* is the “shifted” internal energy [48], computed as

$$u^* = u - u_0 = u - \sum_{i=1}^{n_s} Y_i b_{i0}, \quad (5.2)$$

such that $u^* > 0$ if and only if $T > 0$, provided $c_{v,i} > 0$, $i = 1, \dots, n_s$ [60]. Pressure is then also positive. Note that $C_i > 0$, $\forall i$, implies $\rho > 0$. This set is similar to that in [45,46], except with the additional entropy constraint. In Appendix A, we show that $\rho u^*(y)$ is a concave function of the state. Then, since $s(y)$ is quasi-concave [36, Lemma 2.1] and $s(\bar{y}_\kappa) \geq \min_{x \in \kappa} s(y(x))$ [36, Lemma 2.2], for a given σ , \mathcal{G}_σ is a convex set [34,35,48,85]. We assume that the exact solution to the classical Riemann problem with initial data

$$y(x, 0) = \begin{cases} y_1, & x < 0 \\ y_2, & x > 0 \end{cases}$$

is an entropy solution that preserves positivity. Then, by Lemma 2.2 in [36] and Lemma 9, \mathcal{G}_σ is an invariant set [39,86], i.e., $y_1 \in \mathcal{G}_\sigma$ and $y_2 \in \mathcal{G}_\sigma$ imply that the average of the exact Riemann solution over a domain that includes the Riemann fan [86] is in \mathcal{G}_σ .

Consider the following three-point system arising from a $p = 0$, element-local DG discretization with forward Euler time stepping:

$$y_\kappa^{j+1} = y_\kappa^j - \frac{\Delta t}{h} \left[\mathcal{F}^\dagger \left(y_\kappa^j, y_{\kappa_L}^j, -1 \right) + \mathcal{F}^\dagger \left(y_\kappa^j, y_{\kappa_R}^j, 1 \right) \right], \quad (5.3)$$

where j indexes the time step, h is the element size, and κ_L and κ_R are the elements to the left and right of κ , respectively. Let λ be an upper bound on the maximum wave speed of the system. Under the following condition,

$$\frac{\Delta t \lambda}{h} \leq \frac{1}{2}, \quad (5.4)$$

$y_\kappa^j, y_{\kappa_L}^j, y_{\kappa_R}^j \in \mathcal{G}_\sigma$ implies $y_\kappa^{j+1} \in \mathcal{G}_\sigma$ if certain *invariant-region-preserving* numerical fluxes are employed [22]. In particular, y_κ^{j+1} satisfies [22,85]

$$s(y_\kappa^{j+1}) \geq \min \left\{ s(y_{\kappa_L}^j), s(y_\kappa^j), s(y_{\kappa_R}^j) \right\}. \quad (5.5)$$

The Godunov, Lax-Friedrichs, HLL, and HLLC fluxes qualify [22] (see also [80,17,16,87] for additional proofs regarding the Godunov and/or Lax-Friedrichs fluxes), some of which allow for less restrictive time-step-size constraints than (5.4). The proofs often rely on the notion that \mathcal{G}_σ is an invariant set, which itself invokes the aforementioned assumption that the exact Riemann solution is an entropy solution satisfying the positivity property. Two exceptions are the proof by Zhang and Shu [20] of the positivity property of the Lax-Friedrichs flux and the proof by Lax [88] that the Lax-Friedrichs flux satisfies a discrete cell entropy inequality for all entropy/entropy-flux pairs, from which a sharper version of the inequality (5.5) follows [80,16] (note that the corresponding time-step-size constraints for these two proofs are not necessarily the same as (5.4)). Unless otherwise specified, we employ the HLLC numerical flux [89].

The three-point system (5.3) will be crucial in the construction of a positivity-preserving and entropy-bounded DG scheme for $p > 0$. Specifically, we will show in the following subsection that the element average of the solution (for $p > 0$) at the next time step, \bar{y}_κ^{j+1} , can be expressed as a convex combination of both pointwise values of $y_\kappa^j(x)$ and three-point systems involving pointwise values of $y_\kappa^j(x)$. If all of said pointwise values of $y_\kappa^j(x)$ are in \mathcal{G}_σ , then \bar{y}_κ^{j+1} will also be in \mathcal{G}_σ under a time-step-size constraint. A simple limiter, described in Section 5.2.1, is applied to ensure that the pointwise values of $y_\kappa^j(x)$ are in \mathcal{G}_σ .

5.2. Entropy-bounded, high-order discontinuous Galerkin method in one dimension

Suppose $\kappa = [x_L, x_R]$. Let x_q and w_q denote the quadrature points and weights, respectively, of a quadrature rule with $x_q \in \kappa$, $w_q > 0$, and $\sum_{q=1}^{n_q} w_q = 1$, where n_q is the number of quadrature points/weights. This set of quadrature points does not need to include the endpoints, and the quadrature rule need not be explicitly used to evaluate any integrals in Equation (3.2). For now, we assume that standard flux interpolation, as in Equation (3.8), is employed; Section 5.2.2 discusses how to account for the modified flux interpolation in Equation (3.9). As in [17], provided that the quadrature rule is sufficiently accurate, the element-averaged solution in Equation (3.7) can be expanded as

$$\begin{aligned} \bar{y}_\kappa &= \sum_{q=1}^{n_q} w_q y_\kappa(x_q) \\ &= \sum_{q=1}^{n_q} \theta_q y_\kappa(x_q) + \theta_L y_\kappa(x_L) + \theta_R y_\kappa(x_R). \end{aligned} \quad (5.6)$$

If the set of quadrature points includes the endpoints, then we can simply take

$$\theta_q = \begin{cases} w_q & x_q \neq x_L, x_q \neq x_R \\ 0 & \text{otherwise} \end{cases}$$

and

$$\theta_L = w_L, \quad \theta_R = w_R,$$

where w_L and w_R are the quadrature weights at the left and right endpoints, respectively. If the set of quadrature points does not include the endpoints, then we can instead take

$$\theta_q = w_q - \theta_L \psi_q(x_L) - \theta_R \psi_q(x_R),$$

where $\{\psi_1, \dots, \psi_{n_d}\}$, with $n_b \leq n_d \leq n_q$, is a set of Lagrange basis functions whose nodes are located at a subset of the quadrature points, while $\psi_v = 0$ for $v = n_d + 1, \dots, n_q$, such that [17]

$$\begin{aligned} \sum_{q=1}^{n_q} \theta_q y_k(x_q) &= \sum_{q=1}^{n_q} [w_q - \theta_L \psi_q(x_L) - \theta_R \psi_q(x_R)] y_k(x_q) \\ &= \sum_{q=1}^{n_q} w_q y_k(x_q) - \theta_L \sum_{q=1}^{n_q} y_k(x_q) \psi_q(x_L) - \theta_R \sum_{q=1}^{n_q} y_k(x_q) \psi_q(x_R) \\ &= \sum_{q=1}^{n_q} w_q y_k(x_q) - \theta_L y_k(x_L) + \theta_R y_k(x_R). \end{aligned}$$

θ_L and θ_R will be related to a constraint on the time step size later in this section. The positivity of the quadrature weights guarantees the existence of positive θ_L and θ_R that yield $\theta_q \geq 0$, $q = 1, \dots, n_q$ [17]. Furthermore, $\sum_q \theta_q + \theta_L + \theta_R = 1$ since $\sum_q \psi_q = 1$. Define $\partial D_\kappa = \{x_L, x_R\}$, and let D_κ denote the set of points at which the state is evaluated in Equation (5.6):

$$D_\kappa = \partial D_\kappa \cup \{x_q, q = 1, \dots, n_q\} = \{x_L, x_R, x_q, q = 1, \dots, n_q\}.$$

Applying forward Euler time stepping to Equation (3.2) and taking \mathbf{v} to be a vector of ones (i.e., $\mathbf{v} \in V_h^0$) gives the fully discrete scheme satisfied by the element averages [36,17]:

$$\bar{y}_\kappa^{j+1} = \bar{y}_\kappa^j - \frac{\Delta t}{h} \left[\mathcal{F}^\dagger(y_\kappa^j(x_L), y_{\kappa_L}^j(x_L), -1) + \mathcal{F}^\dagger(y_\kappa^j(x_R), y_{\kappa_R}^j(x_R), 1) \right] \quad (5.7)$$

$$\begin{aligned} &= \sum_{q=1}^{n_q} \theta_q y_\kappa^j(x_q) + \theta_L y_\kappa^j(x_L) - \frac{\Delta t}{h} \left[\mathcal{F}^\dagger(y_\kappa^j(x_L), y_{\kappa_L}^j(x_L), -1) + \mathcal{F}^\dagger(y_\kappa^j(x_L), y_\kappa^j(x_R), 1) \right] \\ &\quad + \theta_R y_\kappa^j(x_R) - \frac{\Delta t}{h} \left[\mathcal{F}^\dagger(y_\kappa^j(x_R), y_{\kappa_R}^j(x_R), 1) + \mathcal{F}^\dagger(y_\kappa^j(x_R), y_\kappa^j(x_L), -1) \right], \end{aligned} \quad (5.8)$$

where the second equality is due to the conservation property of the numerical flux:

$$\mathcal{F}^\dagger(y_\kappa^j(x_L), y_\kappa^j(x_R), 1) = -\mathcal{F}^\dagger(y_\kappa^j(x_R), y_\kappa^j(x_L), -1).$$

Note that Equations (5.7) and (5.8) hold regardless of whether the integrals in Equation (3.2) are evaluated using conventional quadrature or a quadrature-free implementation [76,77]. Though the forward Euler time integration scheme is used here, strong-stability-preserving Runge-Kutta (SSPRK) methods [90,91], which are convex combinations of forward Euler steps, are compatible as well. These methods are typically employed due to their higher accuracy than the forward Euler scheme (in the transport step) [68–73]. Equation (5.8) then leads to the following theorem, where we use y_κ^- to denote the exterior state along $\partial \kappa$.

Theorem 1 ([20,36,17]). If $y_\kappa^j(x) \in \mathcal{G}_\sigma$, $\forall x \in D_\kappa$, and $y_\kappa^{-j} \in \mathcal{G}_\sigma$, $\forall x \in \partial D_\kappa$, with

$$\sigma \leq \min \left\{ \min \{s(y_\kappa^j(x)) \mid x \in D_\kappa\}, \min \{s(y_\kappa^{-j}(x)) \mid x \in \partial D_\kappa\} \right\}, \quad (5.9)$$

then \bar{y}_κ^{j+1} in Equation (5.7) is also in \mathcal{G}_σ under the constraint

$$\frac{\Delta t \lambda}{h} \leq \frac{1}{2} \min \{\theta_L, \theta_R\} \quad (5.10)$$

and the conditions

$$\theta_L > 0, \theta_R > 0, \theta_q \geq 0, q = 1, \dots, n_q. \quad (5.11)$$

Proof. The proof follows the same procedure as in [20], [36], [17], and related papers, which we review here. We first rewrite Equation (5.8) as

$$\bar{y}_\kappa^{j+1} = \sum_{q=1}^{n_q} \theta_q y_\kappa^j(x_q) + \theta_L y_{\kappa,s1}^{j+1} + \theta_R y_{\kappa,s2}^{j+1},$$

where

$$y_{\kappa,s1}^{j+1} = y_\kappa^j(x_L) - \frac{\Delta t}{\theta_L h} \left[\mathcal{F}^\dagger(y_\kappa^j(x_L), y_{\kappa_L}^j(x_L), -1) + \mathcal{F}^\dagger(y_\kappa^j(x_L), y_\kappa^j(x_R), 1) \right],$$

$$y_{\kappa,s2}^{j+1} = y_\kappa^j(x_R) - \frac{\Delta t}{\theta_R h} \left[\mathcal{F}^\dagger(y_\kappa^j(x_R), y_\kappa^j(x_L), -1) + \mathcal{F}^\dagger(y_\kappa^j(x_R), y_{\kappa_R}^j(x_R), 1) \right].$$

As such, \bar{y}_κ^{j+1} is a convex combination of $y_\kappa^j(x_q)$ evaluated at x_q and two three-point systems of the type (5.3). Under the conditions (5.10) and (5.11), $y_{\kappa,s1}^{j+1}$ and $y_{\kappa,s2}^{j+1}$ are both in \mathcal{G}_σ . It then follows that $\bar{y}_\kappa^{j+1} \in \mathcal{G}_\sigma$. \square

Remark 2. A direct result of Theorem 1 is that

$$s(\bar{y}_\kappa^{j+1}) \geq \min \{ \min \{ s(y_\kappa^j(x)) \mid x \in D_\kappa \}, \min \{ s(y_\kappa^{-j}(x)) \mid x \in \partial D_\kappa \} \}.$$

According to the inequality (5.10), the upper bound on the time step size is proportional to $\min \{ \theta_L, \theta_R \}$. For Gauss-Lobatto quadrature, θ_L and θ_R are both equal to the quadrature weight corresponding to either endpoint. See [17] for information about Gauss-Legendre quadrature, as well as a discussion on how to find the maximum allowable value of $\min \{ \theta_L, \theta_R \}$ for general quadrature rules.

To complete the construction of an entropy-bounded, high-order DG scheme, we need to enforce not only the positivity of $y_\kappa^{j+1}(x)$, $\forall x \in D_\kappa$, for all $\kappa \in \Omega$, but also $s(y_\kappa^{j+1}(x)) > s_b$, $\forall x \in D_\kappa$, for all $\kappa \in \Omega$, where s_b is a lower bound on the specific thermodynamic entropy. s_b can vary among elements and time steps, and the prescription of s_b should be motivated by the physical principles examined in Section 4. We will discuss s_b in more detail in Section 5.2.3. In other words, we enforce $y_\kappa^{j+1}(x) \in \mathcal{G}_{s_b}$, $\forall x \in D_\kappa$, which is done via a simple limiting procedure that will be described in Section 5.2.1.

In practice, we relax some of the requirements introduced thus far. First, λ is computed in a local (instead of global) manner and is calculated as the maximum value of $|v| + c$, where c is the speed of sound, over the points of interest. However, $|v| + c$ does not bound the wave speeds arising from the interactions between states at interfaces. A similar remark can be made for most invariant-region-preserving numerical flux functions, which typically require wave-speed estimates. Simple algorithms for bounding the wave speeds in the monocomponent case have been developed [92,93]; extending these to the multicomponent Euler equations may indeed be worthy of future investigation, with [94] as one example. Second, we introduce $\chi_\sigma = \rho s - \rho \sigma$, which is concave with respect to the state [22], and revise the definition of \mathcal{G}_σ as

$$\mathcal{G}_\sigma = \left\{ y \mid \rho > 0, \rho u^* > 0, C_1 \geq 0, \dots, C_{n_s} \geq 0, \chi_\sigma \geq 0 \right\}, \quad (5.12)$$

where $\chi_\sigma \geq 0$ is a reformulation of $s \geq \sigma$ and the species concentrations are now allowed to be equal to zero. From a practical standpoint, allowing $C_i = 0$ is necessary since the concentrations are frequently zero in many reacting flow problems of interest. Unfortunately, entropy functions of the form $U = -\rho f_e(s)$ and $U = -\rho s$ are no longer convex if any of the concentrations is zero [16, 51]. Furthermore, the specific thermodynamic entropy becomes ill-defined. Nevertheless, by making use of $0 \log 0 = 0$ [60, Chapter 6], ρs and thus χ_σ remain well-defined. The entire methodology developed here also remains well-defined, unlike entropy-stable schemes that rely on the entropy variables associated with $U = -\rho s$. Throughout this work, we did not encounter any major issues associated with relaxing the two aforementioned requirements. One potential reason is that \bar{y}_κ^{j+1} can be in \mathcal{G}_σ even if \mathcal{G}_σ is not convex and/or some of the conditions in Theorem 1 are not satisfied. Furthermore, in this work, we choose CFL = 0.1, where [95]

$$\text{CFL} = \frac{\Delta t (2p + 1)}{h} (|v| + c),$$

to maintain low temporal errors, particularly for the grid convergence studies in Sections 8.1 and 8.2. This generally yields a smaller time step size than necessary. Should issues emerge in future work, they can likely be alleviated by adaptively decreasing the time step size [35].

Finally, we remark that D_κ is simply the set of points at which limiting should be applied. Specifically, the interior quadrature points in D_κ need not be explicitly used in numerical integrations in Equation (3.2); if they are indeed not, the actual integration points are added to D_κ as well [35].

5.2.1. Limiting procedure

In this subsection, we describe the limiting procedure to ensure $y_\kappa^{j+1}(x) \in \mathcal{G}_{s_b}$, $\forall x \in D_\kappa$. It is assumed that $\bar{y}_\kappa^{j+1}(x) \in \mathcal{G}_{s_b}$. For brevity, we drop the $j + 1$ superscript and κ subscript in this discussion. The limiting operator is of the same form as in [44], [35], [22], [85], and related papers.

1. First, positivity of density is enforced. Specifically, if $\rho(x) > \epsilon$, $\forall x \in D_\kappa$, where ϵ is a small positive number (e.g., $\epsilon = 10^{-10}$), then set $C_i^{(1)} = C_i = \sum_{j=1}^{n_b} C_i(x_j) \phi_j$, $i = 1, \dots, n_s$; otherwise, compute

$$C_i^{(1)} = \bar{C}_i + \theta^{(1)} (C_i - \bar{C}_i), \quad i = 1, \dots, n_s,$$

with

$$\theta^{(1)} = \frac{\rho(\bar{y}) - \epsilon}{\rho(\bar{y}) - \min_{x \in D} \rho(y(x))}.$$

Note that although $\epsilon = 10^{-10}$ is adequate for the test cases considered in this work, appropriate selection of ϵ may be problem-dependent.

2. Next, nonnegativity of the species concentrations is enforced. If $C_i^{(1)}(x) \geq 0$, $\forall x \in D_\kappa$, then set $C_i^{(2)} = C_i^{(1)}$, $i = 1, \dots, n_s$; otherwise, compute

$$C_i^{(2)} = \bar{C}_i + \theta^{(2)} (C_i^{(1)} - \bar{C}_i), \quad i = 1, \dots, n_s,$$

with

$$\theta^{(2)} = \frac{\bar{C}_i}{\bar{C}_i - \min_{x \in D} C_i^{(1)}(x)}.$$

Let $y^{(2)} = (\rho v_1, \dots, \rho v_d, \rho e, C_1^{(2)}, \dots, C_{n_s}^{(2)})$. Although Step 1 may seem redundant, Step 2 alone does not guarantee positive density. For example, consider a two-species case where both species concentrations are negative at the same point in D_κ . Without Step 1, Step 2 would correct the concentrations at that point to zero, resulting in zero density.

3. Positivity of $\rho u^*(y)$ is then enforced. If $\rho u^*(y^{(2)}(x)) > \epsilon$, $\forall x \in D_\kappa$, then set $y^{(3)} = y^{(2)}$; otherwise, compute

$$y^{(3)} = \bar{y} + \theta^{(3)} (y^{(2)} - \bar{y}),$$

with

$$\theta^{(3)} = \frac{\rho u^*(\bar{y}) - \epsilon}{\rho u^*(\bar{y}) - \min_{x \in D} \rho u^*(y^{(2)}(x))}.$$

It can be shown that $\rho u^*(y^{(3)}(x)) > 0$, $\forall x \in D_\kappa$ by concavity [44,35]. The “positivity-preserving limiter” refers to the limiting procedure up to this point. The “entropy limiter” corresponds to the following step (in addition to the above steps).

4. Finally, the entropy constraint is enforced. If $\chi(y^{(3)}(x)) \geq 0$, $\forall x \in D_\kappa$, then set $y^{(4)} = y^{(3)}$; otherwise, compute

$$y^{(4)} = \bar{y} + \theta^{(4)} (y^{(3)} - \bar{y}),$$

with

$$\theta^{(4)} = \frac{\chi(\bar{y})}{\chi(\bar{y}) - \min_{x \in D} \chi(y^{(3)}(x))}.$$

It can be shown that $s(y^{(4)}(x)) \geq s_b$, $\forall x \in D_\kappa$, by concavity of χ [22,85].

$y^{(4)}$ then replaces y as the solution. The limiting operator is conservative, maintains stability, and in general preserves the formal order of accuracy for smooth solutions [20,35,36,17,22]. There is extensive empirical evidence demonstrating preservation of accuracy (see previously cited references, as well as [46], [85], and related papers). However, the order of accuracy can potentially deteriorate when the element average is close to the boundary of \mathcal{G}_{s_b} [35,22]. Furthermore, the linear scaling is not expected to suppress all oscillations [20,22,17,85]. The limiting procedure described here is applied at the end of every RK stage.

5.2.2. Modified flux interpolation

We now discuss how to account for over-integration with the modified flux interpolation in Equation (3.9). The scheme satisfied by the element averages becomes

$$\begin{aligned} \bar{y}_\kappa^{j+1} &= \bar{y}_\kappa^j - \frac{\Delta t}{h} \left[\mathcal{F}^\dagger \left(\tilde{y}_\kappa^j(x_L), \tilde{y}_{\kappa_L}^j(x_L), -1 \right) + \mathcal{F}^\dagger \left(\tilde{y}_\kappa^j(x_R), \tilde{y}_{\kappa_R}^j(x_R), 1 \right) \right] \\ &= \sum_{q=1}^{n_q} \theta_q y_\kappa^j(x_q) + \theta_L y_\kappa^j(x_L) - \frac{\Delta t}{h} \left[\mathcal{F}^\dagger \left(\tilde{y}_\kappa^j(x_L), \tilde{y}_{\kappa_L}^j(x_L), -1 \right) + \mathcal{F}^\dagger \left(\tilde{y}_\kappa^j(x_L), \tilde{y}_\kappa^j(x_R), 1 \right) \right] \\ &\quad + \theta_R y_\kappa^j(x_R) - \frac{\Delta t}{h} \left[\mathcal{F}^\dagger \left(\tilde{y}_\kappa^j(x_R), \tilde{y}_\kappa^j(x_L), -1 \right) + \mathcal{F}^\dagger \left(\tilde{y}_\kappa^j(x_R), \tilde{y}_{\kappa_R}^j(x_R), 1 \right) \right]. \end{aligned} \quad (5.13)$$

Equation (5.13) can be rewritten as

$$\bar{y}_\kappa^{j+1} = \sum_{q=1}^{n_q} \theta_q y_\kappa^j(x_q) + \theta_L y_{\kappa,s3}^{j+1} + \theta_R y_{\kappa,s4}^{j+1},$$

where

$$y_{\kappa,s3}^{j+1} = y_\kappa^j(x_L) - \frac{\Delta t}{\theta_L h} \left[F^\dagger \left(\tilde{y}_\kappa^j(x_L), \tilde{y}_{\kappa_L}^j(x_L), -1 \right) + F^\dagger \left(\tilde{y}_\kappa^j(x_L), \tilde{y}_{\kappa_R}^j(x_R), 1 \right) \right],$$

$$y_{\kappa,s4}^{j+1} = y_\kappa^j(x_R) - \frac{\Delta t}{\theta_R h} \left[F^\dagger \left(\tilde{y}_\kappa^j(x_R), \tilde{y}_{\kappa_L}^j(x_L), -1 \right) + F^\dagger \left(\tilde{y}_\kappa^j(x_R), \tilde{y}_{\kappa_R}^j(x_R), 1 \right) \right],$$

which are not necessarily of the type (5.3) since in general, $y_\kappa^j(x_L) \neq \tilde{y}_\kappa^j(x_L)$ and $y_\kappa^j(x_R) \neq \tilde{y}_\kappa^j(x_R)$. The incompatibility is a result of expressing \bar{y}_κ as a convex combination of pointwise values of $y_\kappa(x)$ (as opposed to $\tilde{y}_\kappa(x)$). Unfortunately, the element average of \tilde{y}_κ , denoted $\bar{\tilde{y}}_\kappa$, is not necessarily equal to \bar{y}_κ ; consequently, \bar{y}_κ cannot be directly written as a convex combination of pointwise values of $\tilde{y}_\kappa(x)$. However, if the set of solution nodes includes the endpoints (e.g., equidistant or Gauss-Lobatto points), then Equation (5.13) recovers Equation (5.8) since $y_\kappa^j(x_L) = \tilde{y}_\kappa^j(x_L)$ and $y_\kappa^j(x_R) = \tilde{y}_\kappa^j(x_R)$. The previous analysis, including Theorem 1, then holds. As such, for a nodal set that includes the endpoints, the modified flux interpolation in Equation (3.9) does not introduce any additional difficulties to the discussed framework. Note also that the second term in Equation (3.2) (i.e., the volumetric flux integral) does not factor into the scheme satisfied by the element averages, so the modified flux interpolation can be freely employed in said integral.

5.2.3. Lower bound on specific thermodynamic entropy

We consider two options for specifying s_b . The first option is a *global* entropy bound [36,22,85]:

$$s_b(y) = \min \{ s(y(x)) \mid x \in \Omega \}, \quad (5.14)$$

which can be evaluated once based on the initial condition, $y_0(x)$, or updated at each time step [16]. Instead of calculating the true minimum via, for example, Newton's method, we compute

$$s_b(y) = \min \left\{ s(y(x)) \mid x \in \bigcup_{\kappa \in \mathcal{T}} D_\kappa \right\}. \quad (5.15)$$

s_b can also be prescribed by the user if, for example, the minimum entropy of the exact solution is known a priori.

The second option is a *local* entropy bound, which should satisfy

$$s_{b,\kappa}^{j+1}(y) \leq \min \left\{ \min \{ s(y_\kappa^j(x)) \mid x \in D_\kappa \}, \min \{ s(y_\kappa^{-j}(x)) \mid x \in \partial D_\kappa \} \right\},$$

in order to ensure compatibility with Theorem 1 and the limiting procedure, which enforces $y_\kappa^{j+1}(x) \in \mathcal{G}_{s_{b,\kappa}^{j+1}}, \forall x \in D_\kappa$. Lv and Ihme [17] introduced the following local entropy bound:

$$s_{b,\kappa}^{j+1}(y) = \min \left\{ \min \{ s(y_\kappa^j(x)) \mid x \in \kappa \}, \min \{ s(y_\kappa^{-j}(x)) \mid x \in \partial \kappa \} \right\}. \quad (5.16)$$

They demonstrated that the local entropy bound (5.16) can more effectively dampen overshoots and undershoots when the entropy varies significantly throughout the domain (e.g., when multiple discontinuities are present). However, we find that Equation (5.16) is often too restrictive, as will be illustrated in Section 8.1.

Here, we employ a different local entropy bound,

$$s_{b,\kappa}^{j+1}(y) = \min \{ s(y^j(x)) \mid x \in \kappa \cup \kappa_L \cup \kappa_R \}, \quad (5.17)$$

which is based on the local minimum entropy principle satisfied by exact entropy solutions (or discrete entropy solutions in the limit of infinite resolution). Specifically, the inequality

$$s(y(x, t)) \geq \min \{ s(y(x, t_0)) \mid x \in \kappa \cup \kappa_L \cup \kappa_R \}, \quad t \in [t_0, t_0 + \Delta t], \quad (5.18)$$

can be considered the semi-discrete analog of (4.6) with $R = h/2$ and $\kappa = [-h/2, h/2]$, under the condition

$$\frac{\Delta t v_{\max}}{h} \leq 1. \quad (5.19)$$

The RHS of Equation (5.17) is the fully discrete analog of the RHS of the inequality (5.18). This property is imposed on the discrete solution as a means to suppress instabilities. A similar bound was employed by Dzanic and Witherden [96] and Trojak and Dzanic [97] in their entropy-based filtering framework. Note that if Δt satisfies (5.10), then it also satisfies (5.19) since

$$\Delta t \leq \frac{h}{2\lambda} \min \{ \theta_L, \theta_R \} \leq \frac{h}{2\lambda} \leq \frac{h}{\lambda} \leq \frac{h}{v_{\max}}.$$

An alternate viewpoint draws from the generalized Riemann problem (GRP) [89], which differs from the *classical* Riemann problem by allowing for source terms and piecewise smooth (as opposed to piecewise constant) initial conditions. Suppose that y_{κ_L} and y_κ form the initial conditions of a GRP centered at x_L , while y_κ and y_{κ_R} form the initial conditions of a GRP centered at

x_R . Under the (potentially strong) assumption that exact solutions (y_L^{GRP} and y_R^{GRP} , respectively) to the GRPs exist, as well as the assumption that those solutions satisfy all entropy inequalities, the exact solution in κ , y_κ^{ex} , arising from the GRPs satisfies [78]

$$\int_{\kappa} U(y_\kappa^{\text{ex}}(x, t)) \leq \int_{\kappa} U(y_\kappa(x, t_0)) dx - \int_{t_0}^t \mathcal{F}^s(y_R^{\text{GRP}}(x_R, \tau)) d\tau + \int_{t_0}^t \mathcal{F}^s(y_L^{\text{GRP}}(x_L, \tau)) d\tau,$$

at least before the local Riemann problems interact [98]. With $(U, \mathcal{F}^s) = (-\rho f_0(s), -\rho v_1 f_0(s))$ and $s_0 = \min\{s(y(x, t_0)) \mid x \in \kappa \cup \kappa_L \cup \kappa_R\}$, the above inequality becomes

$$\begin{aligned} \int_{\kappa} \rho(y_\kappa^{\text{ex}}(x, t)) f_0(s(y_\kappa^{\text{ex}}(x, t))) dx &\geq \int_{\kappa} \rho(y_\kappa(x, t_0)) \min\{s(y_\kappa(x, t_0)) - s_0, 0\} dx \\ &\quad - \int_{t_0}^t \rho v_1(y_R^{\text{GRP}}(x_R, \tau)) \min\{s(y_R^{\text{GRP}}(x_R, \tau)) - s_0, 0\} dx \\ &\quad + \int_{t_0}^t \rho v_1(y_L^{\text{GRP}}(x_L, \tau)) \min\{s(y_L^{\text{GRP}}(x_L, \tau)) - s_0, 0\} dx, \end{aligned}$$

where the first term on the RHS clearly vanishes and the second and third terms vanish due to Equation (4.6). As such, we have $s(y_\kappa^{\text{ex}}(x, t)) \geq s_0$. This property is then imposed on the discrete solution via the local entropy bound in Equation (5.17).

To our knowledge, it is unclear whether the assumption that exact solutions to the GRP exist is valid (even for calorically perfect gases, let alone mixtures of thermally perfect gases). Semi-analytical methods for solving GRPs have been developed; see [89, Chapter 19] for a detailed description and [99] for a comparison of such methods. Discussions on exact solutions to the classical Riemann problem for mixtures of thermally perfect gases can be found in [100,101].

To avoid finding the true minimum over a given element via an iterative procedure, we relax Equation (5.17) and instead compute

$$s_{b,\kappa}^{j+1}(y) = c \min\{s(y^j(x)) \mid x \in \mathcal{D}_\kappa \cup \mathcal{D}_{\kappa_L} \cup \mathcal{D}_{\kappa_R}\}, \quad (5.20)$$

where $c \in (0, 1]$ is a relaxation parameter. The entropy limiter in Section 5.2.1 remains valid since

$$s(\bar{y}_\kappa^{j+1}) \geq \min\{s(y^j(x)) \mid x \in \mathcal{D}_\kappa \cup \mathcal{D}_\kappa^-\} \geq \min\{s(y^j(x)) \mid x \in \mathcal{D}_\kappa \cup \mathcal{D}_{\kappa_L} \cup \mathcal{D}_{\kappa_R}\} \geq s_{b,\kappa}^{j+1}(y).$$

For $c < 1$, it can be useful to simultaneously account for a well-defined global entropy bound, s_b , as

$$s_{b,\kappa}^{j+1}(y) = \max\left\{s_b, c \min\{s(y^j(x)) \mid x \in \mathcal{D}_\kappa \cup \mathcal{D}_{\kappa_L} \cup \mathcal{D}_{\kappa_R}\}\right\}. \quad (5.21)$$

In this work, we simply choose $c = 1$. An alternative approach for estimating the true minimum in an algebraic manner can be found in [17]. Note that Equation (5.20) with $c = 1$ yields the true minimum for $p = 1$ if the solution nodes are located at the endpoints and included in \mathcal{D}_κ . For $\kappa = [x_L, x_R]$, the basis functions are given by

$$\phi_1(x) = \frac{x_R - x}{x_R - x_L}, \phi_2(x) = \frac{x - x_L}{x_R - x_L},$$

such that $\phi_1 + \phi_2 = 1$ and $\phi_i(x) \in (0, 1)$, $\forall x \in (x_L, x_R)$. Therefore, $y_\kappa(x) = y_\kappa(x_1)\phi_1(x) + y_\kappa(x_2)\phi_2(x)$ is a convex combination of the endpoint values of the solution. Then, by Lemma 2.1 in [36], $\min_x s(y_\kappa(x)) = \min\{s(y_\kappa(x_1)), s(y_\kappa(x_2))\}$. This is similarly true in two and three dimensions.

5.2.4. Artificial viscosity

As will be demonstrated in Section 8.3, the proposed entropy-bounded DG method does not completely suppress smaller-scale oscillations, especially in the presence of flow-field discontinuities. Therefore, artificial viscosity is employed in certain test cases in Section 8 to more effectively dampen such oscillations. Specifically, the following dissipation term is added to the LHS of Equation (3.2) [66]:

$$-\sum_{\kappa \in \mathcal{T}} (\mathcal{F}^{\text{AV}}(y, \nabla y), \nabla \mathbf{b})_\kappa, \quad (5.22)$$

where

$$\mathcal{F}^{\text{AV}}(y, \nabla y) = \nu_{\text{AV}} \nabla y,$$

with $\nu_{\text{AV}} \geq 0$ denoting the artificial viscosity. The artificial viscosity is computed as [14]

$$\nu_{\text{AV}} = (C_{\text{AV}} + S_{\text{AV}}) \left(\frac{h^2}{p+1} \left| \frac{\partial T}{\partial y} \cdot \frac{\mathcal{R}(y, \nabla y)}{T} \right| \right).$$

C_{AV} is a user-defined coefficient, S_{AV} is a shock sensor based on intra-element variations [25], and $\mathcal{R}(y, \nabla y)$ is the strong form of the residual (2.1). Note that Equation (5.7) (the scheme satisfied by the element averages) remains the same since the dissipation term (5.22) vanishes for $\mathbf{v} \in V_h^0$. Therefore, Theorem 1 still holds. This type of artificial viscosity was found to effectively suppress spurious oscillations in the vicinity of flow-field discontinuities in multicomponent reacting flows [14]. However, we remark that the artificial-viscosity formulation presented here is not the focus of this paper; other types of artificial viscosity or limiters can be employed to dampen the small-scale instabilities that the linear-scaling limiter fails to cure, provided that the element-local averages are unmodified. Note that unless the artificial viscosity is appropriately bounded, the inclusion of the dissipation term (5.22) can further restrict the time-step size, especially in problems with strong shocks. In this work, the artificial-viscosity formulation is not explicitly taken into account when calculating Δt .

6. Reaction step: entropy-stable discontinuous Galerkin method for ODE integration

In this section, we describe the entropy-stable DG discretization of Equation (3.4) (i.e., the ordinary differential equation (ODE) with stiff chemical source terms). We build on DGODE, the (non-entropy-stable) DG method for ODE integration described in [14]. The local, semi-discrete integral form of Equation (3.4) is given by

$$\int_{\kappa} \mathbf{v}^T \frac{\partial y}{\partial t} dx - \int_{\kappa} \mathbf{v}^T S(y) dx = 0. \quad (6.1)$$

Approximating $S(y)$ locally as a polynomial in V_h^p ,

$$S_{\kappa} \approx \sum_{j=1}^{n_b} S(y(x_j)) \phi_j,$$

we can write

$$\frac{d}{dt} y_{\kappa}(x_j, t) - S(y_{\kappa}(x_j, t)) = 0, \quad j = 1, \dots, n_b,$$

which is a spatially decoupled system of ODEs advanced at the solution nodes from $t = t_0$ to $t = t_f$. Our goal here is to ensure

$$y_{\kappa}(x_j, t_f) \in \mathcal{G}_{s(y_{\kappa}(x_j, t_0))}, \quad j = 1, \dots, n_b.$$

Assuming a Gauss-Lobatto nodal set, since $\bar{y}_{\kappa}(t_f)$ is a convex combination of the nodal values, we have $\bar{y}_{\kappa}(t_f) \in \mathcal{G}_{s_b}$, where s_b is now given by

$$s_b = \min_{j=1, \dots, n_b} s(y_{\kappa}(x_j, t_0)).$$

The limiting procedure described in Section 5.2.1 can then be applied to enforce $y_{\kappa}(x, t_f) \in \mathcal{G}_{s_b}$, $\forall x \in D_{\kappa}$ (unless $D_{\kappa} = \{x_j, j = 1, \dots, n_b\}$, in which case the limiting procedure is unnecessary).

In the following, we drop the “ κ ” and “ j ” subscripts, yielding

$$\frac{dy}{dt} - S(y) = 0, \quad (6.2)$$

which is the system of ODEs solved at each node. Note that the formulation described here is slightly different from that in [12].

6.1. Review: DGODE

We first briefly review DGODE, referred to as “standard DGODE,” which deals with the following one-dimensional DG discretization in time of Equation (6.2):

$$N_h(y, \mathbf{v}) = \sum_{\epsilon \in \mathcal{E}} (y^{\dagger}(y^+, y^-, n), \llbracket \mathbf{v} \rrbracket)_{\epsilon} - \sum_{\kappa \in \mathcal{T}} \left(y, \frac{d\mathbf{v}}{dt} \right)_{\kappa} - \sum_{\kappa \in \mathcal{T}} (S(y), \mathbf{v})_{\kappa} = 0 \quad \forall \mathbf{v} \in V_h^p, \quad (6.3)$$

where ϵ , \mathcal{E} , κ , \mathcal{T} , and V_h^p are temporal analogs of the spatial counterparts defined in Section 3. Specifically, \mathcal{E} is the set of temporal interfaces ϵ , \mathcal{T} is the set of cells κ that partitions the computational domain, $\Omega = (t_0, t_f) = (t_0, t_0 + \Delta t)$, and V_h^p is the discrete subspace defined similarly to Equation (3.1). Note that “cell” in this context corresponds to a sub-time-step (referred to in this section as simply “time step”) of size $\tau \in (0, \Delta t]$. Equation (6.3) is obtained by integrating Equation (6.2) over each cell, performing integration by parts on the time-derivative terms, and summing over the domain. On interior faces, the numerical temporal flux (henceforth referred to as the “numerical state”), y^{\dagger} , is defined as the upwind flux function,

$$y^{\dagger}(y^+, y^-, n) = \begin{cases} y^+ & \text{if } n \geq 0 \\ -y^- & \text{if } n < 0 \end{cases}, \text{ on } \epsilon \quad \forall \epsilon \in \mathcal{E}_I. \quad (6.4)$$

On exterior interfaces, the numerical state is defined as

$$y^\dagger(y^+, y^-, n) = \begin{cases} y^+ & \text{if } n \geq 0 \\ -y_\partial(y^+) & \text{if } n < 0 \end{cases}, \text{ on } \epsilon \quad \forall \epsilon \in \mathcal{E}_\partial, \quad (6.5)$$

where $y_\partial(y^+)$ is a prescribed boundary state. At the inflow interface, located at $t = t_0$, $y_\partial = y_0$, which is the initial condition. At the outflow interface, located at $t = t_f$, $y_\partial = y^+$ (i.e., no boundary condition is imposed).

Let $m = \dim V_h^p$ and (ϕ_1, \dots, ϕ_m) be a basis for V_h^p . The discrete residual, $\mathcal{R} = (\mathcal{R}_1(y), \dots, \mathcal{R}_m(y))$ is defined as

$$\mathcal{R}_i(y) = \sum_{\epsilon \in \mathcal{E}} (y^\dagger(y^+, y^-, n), \llbracket \phi_i \rrbracket)_\epsilon - \sum_{\kappa \in \mathcal{T}} \left(y, \frac{d\phi_i}{dt} \right)_\kappa - \sum_{\kappa \in \mathcal{T}} (S(y), \phi_i)_\kappa \quad (6.6)$$

for $i = 1, \dots, m$. We can then recast (6.3) as

$$\mathcal{R}(y) = 0,$$

which is solved for y via Newton's method. With initial guess y^0 , the k th update, y^k , is computed by solving the linear system

$$\frac{d}{dy} \mathcal{R}(y^k) (y^{k+1} - y^k) = -\mathcal{R}(y^k) \quad (6.7)$$

recursively until a convergence criterion is satisfied.

Johnson and Kercher [14] introduced a simple yet effective adaptation strategy to control both the time step size, τ , and polynomial degree, p . They applied the strategy to efficiently and accurately integrate chemical systems with complex mechanisms. Here, we focus on time-step-adaptation with uniform p . We define the norm of the local error estimate as

$$\text{err}_h = \left\| \frac{\mathcal{R}(y)}{\epsilon_{\text{abs}} + \epsilon_{\text{rel}} |y|} \right\|,$$

where ϵ_{abs} and ϵ_{rel} are user-specified absolute and relative tolerances, respectively. The convergence criterion is

$$\text{err}_h < 1. \quad (6.8)$$

If (6.8) is satisfied within a user-specified number of Newton iterations (chosen to be ten in this work), the solution is updated and a new time step is determined using Gustafsson's method [102]. Otherwise, the time-step size is reduced by a factor of ten.

In this work, given that implicit time stepping schemes with order greater than one are typically not unconditionally positivity-preserving [103], we introduce an additional convergence criterion that improves stability and more robustly maintains conservation of mass:

$$C_i \geq 0, \quad i = 1, \dots, n_s. \quad (6.9)$$

Specifically, both (6.8) and (6.9) must be satisfied in order to update the solution; otherwise, the time-step size is reduced by a factor of ten. In our experience, this additional criterion does not significantly restrict the time-step size. Furthermore, the above criterion can be relaxed. Instead of requiring pointwise nonnegativity of the species concentrations, we can simply require that the spatial averages of the concentrations over the element be nonnegative. Note, however, that using this relaxed criterion had a negligible effect on the solution and cost for the configurations considered in this study. The positivity-preserving limiter in Section 5.2.1 can then be applied to guarantee nonnegativity of the species concentrations in a pointwise manner. Though not pursued in this work, the conservative and positivity-preserving projection method by Sandu [104] can also be employed when (6.9) is violated. Another possible convergence criterion is $T > 0$, but this is almost never a concern.

6.2. Entropy stability: preliminaries

Entropy stability in this ODE setting is defined as

$$U(y(t_f)) \leq U(y_0). \quad (6.10)$$

Here, we consider the entropy function $U = -\rho s$. Combined with discrete mass conservation (i.e., ρ is constant), we have

$$s(y(t_f)) \geq s(y_0). \quad (6.11)$$

In other words, entropy stability implies that the specific thermodynamic entropy is nondecreasing in time, which is in line with the minimum entropy principle.

Standard DGODE, as in Section 6.1, does not necessarily satisfy the inequality (6.10). In the following, we introduce a modified DG discretization that is guaranteed to be entropy-stable.

6.3. Entropy-stable DGODE with summation-by-parts property

We work with the following strong-form discretization, obtained by performing integration by parts on the temporal-derivative term in Equation (6.3):

$$N_h(y, \mathbf{v}) = \sum_{\kappa \in \mathcal{T}} \left[(y^\dagger(y^+, y^-, n) - n \cdot y^+, \mathbf{v}^+)_{\partial\kappa} + \left(\frac{dy}{dt}, \mathbf{v} \right)_\kappa \right] - \sum_{\kappa \in \mathcal{T}} (S(y), \mathbf{v})_\kappa = 0 \quad \forall \mathbf{v} \in V_h^p. \quad (6.12)$$

It is well-known that a collocated DG scheme (i.e., solution nodes and integration points are the same) with Gauss-Lobatto points possesses the diagonal-norm summation-by-parts (SBP) property [54,105,106]. Consider the discrete mass matrix and discrete derivative matrix derived from Gauss-Lobatto collocation, given by

$$\mathbf{M}_{ij} = w_i \delta_{ij}, \quad \mathbf{D}_{ij} = \ell_j'(\xi_i),$$

where w_i is the i th Gauss-Lobatto weight, ℓ_j is the j th Lagrange basis polynomial, and $\xi \in [0, 1]$ is the reference coordinate. \mathbf{M} and \mathbf{D} satisfy the SBP property,

$$\mathbf{Q} + \mathbf{Q}^T = \mathbf{B},$$

where $\mathbf{Q} = \mathbf{M}\mathbf{D}$ and $\mathbf{B} = \text{diag}(-1, 0, \dots, 0, 1)$. The following element-local discrete form is then obtained [18]:

$$\begin{aligned} & \left[y^\dagger(y_\kappa^+, y_\kappa^-, n) - n \cdot y_\kappa^+ \right]^T \mathbf{v}_\kappa^+ \Big|_{\xi=0} + \left[y^\dagger(y_\kappa^+, y_\kappa^-, n) - n \cdot y_\kappa^+ \right]^T \mathbf{v}_\kappa^+ \Big|_{\xi=1} \\ & + \sum_{i=1}^{n_b} w_i \left[\sum_{j=1}^{n_b} \mathbf{D}_{ij} y_\kappa(t_j) - \tau S(y_\kappa(t_i)) \right]^T \mathbf{v}_\kappa(t_i) = 0. \end{aligned} \quad (6.13)$$

Note that in [14], standard DGODE was solved using a quadrature-free approach [76,77]. The discrete form (6.13), though similar, specifically invokes quadrature in order to exploit the SBP property.

We replace the temporal-derivative interpolation operator in Equation (6.13), $\sum_{j=1}^{n_b} \mathbf{D}_{ij} y_\kappa(t_j)$, with a specific temporal-derivative projection operator [18], $2 \sum_{j=1}^{n_b} \mathbf{D}_{ij} y^\ddagger(y_\kappa(t_i), y_\kappa(t_j))$, where $y^\ddagger(y_1, y_2)$ is a two-point numerical state function (distinct from y^\dagger) that is consistent and symmetric. Equation (6.13) thus becomes

$$\begin{aligned} & \left[y^\dagger(y_\kappa^+, y_\kappa^-, n) - n \cdot y_\kappa^+ \right]^T \mathbf{v}_\kappa^+ \Big|_{\xi=0} + \left[y^\dagger(y_\kappa^+, y_\kappa^-, n) - n \cdot y_\kappa^+ \right]^T \mathbf{v}_\kappa^+ \Big|_{\xi=1} \\ & + \sum_{i=1}^{n_b} w_i \left[2 \sum_{j=1}^{n_b} \mathbf{D}_{ij} y^\ddagger(y_\kappa(t_i), y_\kappa(t_j)) - \tau S(y_\kappa(t_i)) \right]^T \mathbf{v}_\kappa(t_i) = 0. \end{aligned} \quad (6.14)$$

With the mean-value numerical state,

$$y^\ddagger(y_L, y_R) = \frac{y_L + y_R}{2}, \quad (6.15)$$

Equation (6.14) recovers Equation (6.13) [106,54].

The discretization (6.14) combined with the mean-value numerical state is not necessarily entropy-stable. Although, as will be shown in Section 6.3.2, the source-term discretization results in destruction of mathematical entropy, the temporal-derivative operator may cause production of mathematical entropy. Entropy stability is achieved only if the entropy destruction due to the source term outweighs the entropy production due to the temporal-derivative operator. In the following, by replacing the mean-value numerical state with a more appropriate numerical state, we will obtain a temporal DG scheme that is guaranteed to be entropy-stable.

6.3.1. Entropy-conservative numerical state function

A key ingredient in the development of an entropy-stable DG scheme is a two-point numerical state function that satisfies the following condition [18]:

$$(\mathbf{v}_R - \mathbf{v}_L)^T y^\ddagger(y_L, y_R) = \mathcal{U}_R - \mathcal{U}_L. \quad (6.16)$$

A numerical state that satisfies (6.16) is *entropy-conservative*. Note that an entropy-conservative numerical *flux* satisfies an analogous condition:

$$(\mathbf{v}_R - \mathbf{v}_L)^T \mathcal{F}^\ddagger(y_L, y_R) = \mathcal{F}_R^p - \mathcal{F}_L^p. \quad (6.17)$$

Gouasmi et al. [51] derived a simple, closed-form entropy-conservative numerical flux for the multicomponent Euler equations with the entropy function $U = -\rho s$. They built on the techniques by Roe [107] originally used to construct an entropy-conservative numerical flux for the monocomponent Euler equations. Said techniques rely on (6.17) as a starting point. An analogous procedure, instead using (6.16) as a starting point, is employed here to derive an entropy-conservative numerical state function.

With $[\![\cdot]\!]$ denoting the jump operator, the entropy conservation condition (6.16) can be expressed as

$$[\![\mathbf{v}]\!]^T y^\ddagger = [\![\mathcal{U}]\!]. \quad (6.18)$$

For consistency with [51], we first work with a re-ordered state vector where the species concentrations are replaced with partial densities:

$$y = \left(\rho_1, \dots, \rho_{n_s}, \rho v_1, \dots, \rho v_d, \rho e_t \right)^T. \quad (6.19)$$

We employ the notation

$$y^{\ddagger} = \left(y_{1,1}^{\ddagger}, \dots, y_{1,n_s}^{\ddagger}, y_{2,1}^{\ddagger}, \dots, y_{2,d}^{\ddagger}, y_3^{\ddagger} \right),$$

where the first n_s components correspond to the partial densities, the next d components correspond to the momentum, and the last component corresponds to the total energy. Let z denote the vector

$$z = \left(\rho_1, \dots, \rho_{n_s}, v_1, \dots, v_d, 1/T \right) = \left(z_{1,1}, \dots, z_{1,n_s}, z_{2,1}, \dots, z_{2,d}, z_3 \right).$$

With the entropy function $U = -\rho s$, the entropy variables and entropy potential are given by

$$v = \left(\frac{g_1 - \frac{1}{2} \sum_{k=1}^d v_k v_k}{T}, \dots, \frac{g_{n_s} - \frac{1}{2} \sum_{k=1}^d v_k v_k}{T}, \frac{v_1}{T}, \dots, \frac{v_d}{T}, -\frac{1}{T} \right)^T, \quad \mathcal{U} = \sum_{i=1}^{n_s} W_i \rho_i.$$

Next, we introduce the arithmetic mean, logarithmic mean, and product operators,

$$\begin{aligned} \{\{\alpha\}\} &= \frac{\alpha_L + \alpha_R}{2}, \\ \alpha^{\ln} &= \begin{cases} \alpha_L, & \text{if } \alpha_L = \alpha_R \\ 0, & \text{if } \alpha_L = 0 \text{ or } \alpha_R = 0 \\ \frac{\alpha_R - \alpha_L}{\ln \alpha_R - \ln \alpha_L}, & \text{otherwise,} \end{cases} \\ \alpha^{\times} &= \alpha_L \alpha_R \end{aligned} \quad (6.20)$$

which are equipped with the identities

$$\begin{aligned} \{\{\alpha\beta\}\} &= \alpha \{\{\beta\}\} + \beta \{\{\alpha\}\} \\ \llbracket \ln \alpha \rrbracket &= \frac{\llbracket \alpha \rrbracket}{\alpha^{\ln}} \\ \llbracket \alpha \rrbracket &= -\alpha^{\times} \left\llbracket \frac{1}{\alpha} \right\rrbracket, \alpha \neq 0. \end{aligned}$$

Note that the three operators in (6.20) are symmetric; the first two are also consistent (the product operator is consistent with α^2). To compute the logarithmic mean in a numerically stable manner, we employ the procedure by Ismail and Roe [108]. The jump in the entropy potential can then be written as

$$\llbracket \mathcal{U} \rrbracket = \sum_{i=1}^{n_s} W_i \llbracket \rho_i \rrbracket = \sum_{i=1}^{n_s} W_i \llbracket z_{1,i} \rrbracket, \quad (6.21)$$

while the jump in the entropy variables, after some algebraic manipulation, can be expressed as [51]

$$\llbracket v \rrbracket = \begin{pmatrix} \llbracket z_3 \rrbracket \times_1 + \llbracket z_{1,1} \rrbracket \frac{W_1}{\rho_1^{\ln}} - \sum_{k=1}^d \llbracket z_{2,k} \rrbracket \left\{ \left\{ \frac{1}{T} \right\} \right\} \left\{ \left\{ v_k \right\} \right\} \\ \vdots \\ \llbracket z_3 \rrbracket \times_{n_s} + \llbracket z_{1,n_s} \rrbracket \frac{W_{n_s}}{\rho_{n_s}^{\ln}} - \sum_{k=1}^d \llbracket z_{2,k} \rrbracket \left\{ \left\{ \frac{1}{T} \right\} \right\} \left\{ \left\{ v_k \right\} \right\} \\ \left\{ \left\{ z_3 \right\} \right\} \llbracket z_{2,1} \rrbracket + \left\{ \left\{ z_{2,1} \right\} \right\} \llbracket z_3 \rrbracket \\ \vdots \\ \left\{ \left\{ z_3 \right\} \right\} \llbracket z_{2,d} \rrbracket + \left\{ \left\{ z_{2,d} \right\} \right\} \llbracket z_3 \rrbracket \\ - \llbracket z_3 \rrbracket \end{pmatrix}, \quad (6.22)$$

where

$$\times_i = b_{i0} + \frac{b_{i1}}{(1/T)^{\ln}} + \sum_{r=2}^{n_p+1} b_{ir} (f_{r-1}(T) T^{\times}) - \frac{1}{2} \sum_{k=1}^d \left\{ \left\{ v_k^2 \right\} \right\},$$

with $f_r(\alpha)$ denoting a special averaging operator, consistent with α^{r-1} , that satisfies $\llbracket \alpha^r \rrbracket = r f_r(\alpha) \llbracket \alpha \rrbracket$. For $r = 1, 2, 3, 4$, $f_r(\alpha)$ is defined as

$$\begin{aligned} f_1(\alpha) &= 1, \\ f_2(\alpha) &= \{\{\alpha\}\}, \\ f_3(\alpha) &= \frac{2}{3} \{\{\alpha\}\} \{\{\alpha\}\} + \frac{1}{3} \{\{\alpha^2\}\}, \end{aligned}$$

$$f_4(\alpha) = \{\{\alpha\}\} \{\{\alpha^2\}\}.$$

$f_r(\alpha)$ can be derived for $r > 4$ as well [51]. Using Equations (6.21) and (6.22), we rewrite the entropy conservation condition in time (6.18) as a requirement that a linear combination of the jumps in the components of z equals zero:

$$\begin{aligned} & \sum_{i=1}^{n_s} \llbracket z_{1,i} \rrbracket \left(y_{1,i}^\ddagger \frac{W_i}{\rho_i^{\ln}} - W_i \right) + \sum_{k=1}^d \llbracket z_{2,k} \rrbracket \left(y_{2,k}^\ddagger \{\{z_3\}\} - \sum_{i=1}^{n_s} y_{1,i}^\ddagger \left\{ \left\{ \frac{1}{T} \right\} \right\} \{\{v_k\}\} \right) \\ & + \llbracket z_3 \rrbracket \left(\sum_{i=1}^{n_s} y_{1,i}^\ddagger X_i + \sum_{k=1}^d y_{2,k}^\ddagger \{\{z_{2,k}\}\} - y_3^\ddagger \right) = 0. \end{aligned}$$

Invoking the independence of these jumps yields a system of m equations:

$$\begin{aligned} y_{1,i}^\ddagger \frac{W_i}{\rho_i^{\ln}} - W_i &= 0, \quad i = 1, \dots, n_s, \\ y_{2,k}^\ddagger \{\{z_3\}\} - \sum_{i=1}^{n_s} y_{1,i}^\ddagger \left\{ \left\{ \frac{1}{T} \right\} \right\} \{\{v_k\}\} &= 0, \quad k = 1, \dots, d, \\ \sum_{i=1}^{n_s} y_{1,i}^\ddagger X_i + \sum_{k=1}^d y_{2,k}^\ddagger \{\{z_{2,k}\}\} - y_3^\ddagger &= 0. \end{aligned}$$

Solving for the components of y^\ddagger then gives

$$y^\ddagger = \begin{pmatrix} \rho_1^{\ln} \\ \vdots \\ \rho_{n_s}^{\ln} \\ \sum_{i=1}^{n_s} \rho_i^{\ln} \{\{v_1\}\} \\ \vdots \\ \sum_{i=1}^{n_s} \rho_i^{\ln} \{\{v_d\}\} \\ \sum_{k=1}^d \sum_{i=1}^{n_s} \rho_i^{\ln} \{\{v_k\}\} \{\{v_k\}\} + \sum_{i=1}^{n_s} \rho_i^{\ln} \left[b_{i0} + \frac{b_{i1}}{(1/T)^{\ln}} + \sum_{r=2}^{n_p+1} b_{ir} (f_{r-1}(T)T^\times) - \frac{1}{2} \sum_{k=1}^d \{\{v_k^2\}\} \right] \end{pmatrix}. \quad (6.23)$$

Note that Equation (6.23) corresponds to the state vector (6.19). A simple re-ordering and linear mapping [51] yields

$$y^\ddagger = \begin{pmatrix} \sum_{i=1}^{n_s} \rho_i^{\ln} \{\{v_1\}\} \\ \vdots \\ \sum_{i=1}^{n_s} \rho_i^{\ln} \{\{v_d\}\} \\ \sum_{k=1}^d \sum_{i=1}^{n_s} \rho_i^{\ln} \{\{v_k\}\} \{\{v_k\}\} + \sum_{i=1}^{n_s} \rho_i^{\ln} \left[b_{i0} + \frac{b_{i1}}{(1/T)^{\ln}} + \sum_{r=2}^{n_p+1} b_{ir} (f_{r-1}(T)T^\times) - \frac{1}{2} \sum_{k=1}^d \{\{v_k^2\}\} \right] \\ C_1^{\ln} \\ \vdots \\ C_{n_s}^{\ln} \end{pmatrix}, \quad (6.24)$$

which corresponds to the original state vector (2.2). We then have the following theorem.

Theorem 3. *The two-point numerical state function in Equation (6.24) is entropy-conservative, consistent, and symmetric.*

Proof. The numerical state (6.24) is entropy-conservative by construction. Since all of the introduced operators are symmetric, the numerical state is symmetric. Finally, recognizing that $f_{r-1}(\alpha)\alpha^\times$ is consistent with α^r , taking the left and right states to be the same yields

$$y^\ddagger = \begin{pmatrix} \rho v_1 \\ \vdots \\ \rho v_d \\ \sum_{k=1}^d \rho v_k v_k + \sum_{i=1}^{n_s} \rho_i \left[b_{i0} + b_{i1}T + \sum_{r=2}^{n_p+1} b_{ir}T^r - \frac{1}{2} \sum_{k=1}^d v_k^2 \right] \\ C_1 \\ \vdots \\ C_{n_s} \end{pmatrix} = \begin{pmatrix} \rho v_1 \\ \vdots \\ \rho v_d \\ \rho u + \frac{1}{2} \rho \sum_{k=1}^d v_k v_k \\ C_1 \\ \vdots \\ C_{n_s} \end{pmatrix} = y.$$

Therefore, it is also consistent. \square

Remark 4. The derived entropy-conservative numerical state function (6.24) can be directly used in entropy-stable space-time DG schemes based on SBP operators [18].

6.3.2. Discrete temporal entropy analysis

We analyze the entropy stability of the proposed temporal DG discretization in the following theorem.

Theorem 5. Consider the DG discretization (6.14). Assume that y^\dagger is the upwind numerical state and y^\ddagger is the entropy-conservative numerical state in (6.24). Then, for the entropy function $U = -\rho s$, the resulting DG discretization is entropy-stable.

Proof. Take \mathbf{v}_κ in (6.14) to be the polynomial interpolant of the entropy variables, such that

$$\mathbf{v}_\kappa(t_j) = \mathbf{v}(y_\kappa(t_j)), \quad j = 1, \dots, n_b,$$

which results in

$$\begin{aligned} & \sum_{\kappa \in \mathcal{T}} \left[[y^\dagger(y_\kappa^+, y_\kappa^-, n) - n \cdot y_\kappa^+]^T \mathbf{v}(y_\kappa^+) \Big|_{\xi=0} + [y^\dagger(y_\kappa^+, y_\kappa^-, n) - n \cdot y_\kappa^+]^T \mathbf{v}(y_\kappa^+) \Big|_{\xi=1} \right] \\ & + \sum_{\kappa \in \mathcal{T}} \left[\sum_{i=1}^{n_b} w_i \left(2 \sum_{j=1}^{n_b} \mathcal{D}_{ij} y^\ddagger(y_\kappa(t_i), y_\kappa(t_j)) - \tau S(y_\kappa(t_i)) \right)^T \mathbf{v}(y_\kappa(t_i)) \right] = 0. \end{aligned} \quad (6.25)$$

We introduce \mathcal{A}_κ and \mathcal{B}_κ , defined as

$$\begin{aligned} \mathcal{A}_\kappa &= [y^\dagger(y^+, y^-, n) - n \cdot y^+]^T \mathbf{v}(y_\kappa^+) \Big|_{\xi=0} + [y^\dagger(y^+, y^-, n) - n \cdot y^+]^T \mathbf{v}(y_\kappa^+) \Big|_{\xi=1} \\ &+ \sum_{i=1}^{n_b} w_i \left[2 \sum_{j=1}^{n_b} \mathcal{D}_{ij} y^\ddagger(y(t_i), y(t_j)) \right]^T \mathbf{v}(y_\kappa(t_i)) \\ \mathcal{B}_\kappa &= - \sum_{i=1}^{n_b} w_i \tau S(y_\kappa(t_i))^T \mathbf{v}(y_\kappa(t_i)), \end{aligned}$$

such that Equation (6.25) can be rewritten as

$$\sum_{\kappa \in \mathcal{T}} \mathcal{A}_\kappa + \sum_{\kappa \in \mathcal{T}} \mathcal{B}_\kappa = 0. \quad (6.26)$$

By invoking the SBP property and the fact that the upwind numerical state function is an entropy-stable numerical state (i.e., it satisfies $[[\mathbf{v}]]^T y^\dagger \leq [[U^*]]$) [18], we obtain the inequality

$$U(y(t_f)) - U(y_0) \leq \sum_{\kappa \in \mathcal{T}} \mathcal{A}_\kappa, \quad (6.27)$$

the proof of which is very similar to that in [18, Theorem 1] (just without any spatial component) and therefore not included here. It remains to analyze $\sum_{\kappa \in \mathcal{T}} \mathcal{B}_\kappa$. The quantity $S(y_\kappa(t_i))^T \mathbf{v}(y_\kappa(t_i))$ is simply the pointwise entropy production rate due to the chemical source terms, which, as demonstrated in Section 4.2, is nonpositive. Since $w_i > 0$ and $\tau > 0$, we have

$$\sum_{\kappa \in \mathcal{T}} \mathcal{B}_\kappa \geq 0. \quad (6.28)$$

Combining Equations (6.26), (6.27), and (6.28) gives the inequality (6.10), which completes the proof. \square

In the following, we refer to the proposed entropy-stable DG discretization as simply “entropy-stable DGODE.”

Remark 6. Entropy-stable DGODE is well-defined for zero concentrations. However, during early iterations of Newton’s method, negative concentrations can occur, making the formulation ill-defined. As a simple remedy, at each Newton iteration, we first obtain a converged solution with the mean-value numerical state (6.15) (using the same convergence criteria as described in Section 6.1). This solution is then used as an initial guess for entropy-stable DGODE, which we find to be sufficiently robust since this initial guess is generally close to the entropy-stable DGODE solution. Other, more sophisticated approaches can be employed as well.

Remark 7. In general, entropy-stable DGODE is more expensive than standard DGODE. Furthermore, when using the latter, we find that the thermodynamic entropy produced by the source terms typically outweighs any thermodynamic entropy destruction caused by the non-entropy-stable mean-value numerical state, at least for the reaction mechanisms used in this study (though it is important to note that this observation may not hold true for significantly different mechanisms). As such, in practice, the following approach can be employed to maximize efficiency:

- Compute a solution with standard DGODE.
- If $s(y(t_f)) \geq s(y_0)$, then proceed. Otherwise, compute a solution with entropy-stable DGODE.

In Section 8.4, however, in order to test the formulation, entropy-stable DGODE alone is used in certain simulations of a one-dimensional, moving detonation wave.

Remark 8. To reduce computational cost, it is common practice, especially for large-scale simulations, to approximate a given chemical reaction as two irreversible forward reactions (as opposed to having forward and reverse reaction rates). However, this strategy can cause appreciable entropy violations [60,109]. A detailed investigation of whether the gains in speed outweigh the loss in accuracy is outside the scope of this study. If such a strategy is employed, then reverting to standard DGODE is the natural course of action. Though not considered in this work, an alternative approach is to use the least-squares-based method by Ream et al. [110] to generate chemical mechanisms involving irreversible reactions that do not cause entropy violations.

7. Summary of formulation

Before presenting the numerical results, we briefly summarize the proposed formulation:

- Spurious pressure oscillations in moving-interface problems are suppressed by employing a modified flux evaluation in which the pressure is approximated as a polynomial of order p and interpolated to the integration points.
- Nonnegative species concentrations, positive density, positive pressure, and bounded specific entropy (in line with the minimum entropy principle) are mathematically guaranteed.
- Either a global or an element-local bound on the entropy can be enforced.
- Operator splitting is used to separate the temporal integration of the convection operator from that of the stiff chemical source term. In the transport step, an invariant-region-preserving flux and a simple linear-scaling limiter are employed.
- In the reaction step, bounded entropy can be maintained with an entropy-stable DG discretization in time.

The resulting formulation is fully conservative, which we will confirm in the following section by computing the errors in mass, total energy, and atom conservation.

8. One-dimensional results

We consider four one-dimensional test cases. The first and second involve the advection of a thermal bubble and a low-density Gaussian wave, respectively. The third case is a shock-tube problem with multiple flow discontinuities. These first three tests comprise nonreacting multicomponent flows. The final case explores sustained detonations formed via an overdriven initialization. Stiff chemical reactions are present in this test. The two-stage SSPRK2 time integration scheme is employed, except in Section 8.2, where the three-stage SSPRK3 scheme is employed. The latter has better accuracy and stability properties than the former [102], which may allow for a larger time-step size, at the cost of an additional stage. A CFL number of 0.1 is used throughout. Note, however, that larger CFL numbers can be employed; indeed, in Part II [19], we compute more complex, multidimensional reacting flows, where computational cost is a much greater concern, with CFL numbers close to unity. All simulations are performed using a modified version of the JENRE® Multiphysics Framework [111,14] that incorporates the developments and extensions described in this work.

8.1. Thermal bubble

We use this smooth flow problem to assess the grid convergence of the entropy-bounded DG method (without artificial viscosity). The order of accuracy of the limiting procedure in Section 5.2.1 is of particular interest. We also compare the local entropy bound in [17] to that proposed here (Equation (5.20)). The initial conditions are as follows:

$$\begin{aligned}
 v &= 1 \text{ m/s}, \\
 Y_{H_2} &= \frac{1}{2} [1 - \tanh(|x| - 10)], \\
 Y_{O_2} &= 1 - Y_{H_2}, \\
 T &= 1200 - 900 \tanh(|x| - 10) \text{ K}, \\
 P &= 1 \text{ bar}.
 \end{aligned} \tag{8.1}$$

The thermodynamic relations for the hydrogen-oxygen mechanism used here are written as

$$\begin{aligned}
 \frac{W_{H_2} c_{p,H_2}(T)}{R^0} &= 3.47 - 0.220\hat{T} + 0.577\hat{T}^2 - 0.194\hat{T}^3 + 0.0210\hat{T}^4, \\
 \frac{W_{H_2} h_{H_2}(T)}{R^0} &= \int \frac{W_{H_2} c_{p,H_2}(\tau) d\tau}{R^0} - 1028.7 \text{ K}, \quad \frac{W_{H_2} s_{H_2}^0}{R^0} = \int \frac{W_{H_2} c_{p,H_2}(\tau) d\tau}{R^0 \tau} - 4.00, \\
 \frac{W_{O_2} c_{p,O_2}(T)}{R^0} &= 3.09 + 1.77\hat{T} - 0.911\hat{T}^2 + 0.243\hat{T}^3 - 0.0242\hat{T}^4,
 \end{aligned}$$

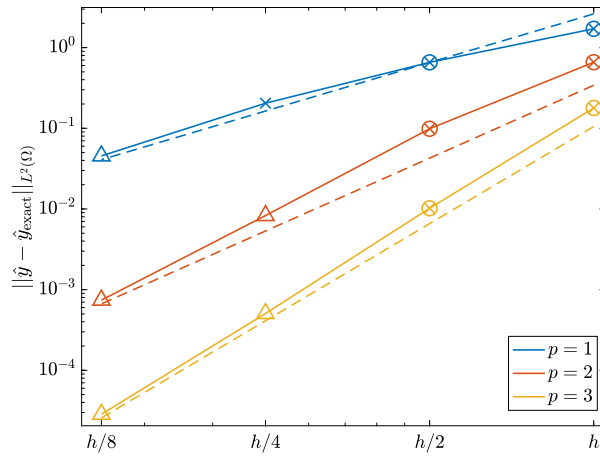


Fig. 8.1. Convergence under grid refinement, with $h = 2$ m, for the one-dimensional thermal bubble test case. The L^2 error of the normalized state with respect to the exact solution at $t = 5$ s is computed. The dashed lines represent the theoretical convergence rates. The “x” marker indicates that the positivity-preserving limiter is activated, the “O” marker indicates that the entropy limiter is activated, and the “Δ” marker indicates that neither limiter is activated. If both limiters are activated, then the corresponding markers are superimposed as “⊗”.

$$\frac{W_{O_2} h_{O_2}(T)}{R^0} = \int \frac{W_{O_2} c_{p,O_2}(\tau) d\tau}{R^0} - 992.9 \text{ K}, \quad \frac{W_{O_2} s_{O_2}^0}{R^0} = \int \frac{W_{O_2} c_{p,O_2}(\tau) d\tau}{R^0 \tau} + 6.57,$$

where $\hat{T} = T/T_r$, with $T_r = 1000$ K, and τ is a dummy variable for T . The computational domain is $\Omega = [-25, 25]$ m, with periodic boundaries. Four element sizes are considered: h , $h/2$, $h/4$, and $h/8$, where $h = 2$ m. Smaller element sizes are not investigated since the limiters are not activated for such fine resolutions and optimal order of accuracy without limiting was already demonstrated in [14]. The L^2 error at $t = 5$ s is calculated in terms of the following normalized state variables:

$$\hat{\rho}v_k = \frac{1}{\sqrt{\rho_r P_r}} \rho v_k, \quad \hat{\rho}e_i = \frac{1}{P_r} \rho e_i, \quad \hat{C}_i = \frac{R^0 T_r}{P_r} C_i,$$

where $\rho_r = 1 \text{ kg}\cdot\text{m}^{-3}$, and $P_r = 101325 \text{ Pa}$ are reference values. The results of the convergence study for $p = 1$ to $p = 3$ are displayed in Fig. 8.1. The dashed lines represent the theoretical convergence rates. The “x” marker indicates that the positivity-preserving limiter is activated, the “O” marker indicates that the entropy limiter is activated, and the “Δ” marker indicates that neither limiter is activated. If both limiters are activated, then the corresponding markers are superimposed as “⊗”. For h and $h/2$, both the positivity-preserving and entropy limiters are engaged regardless of p ; for $h/4$ and $p = 1$, only the positivity-preserving limiter is engaged. That the limiters are no longer activated for well-resolved solutions is a desirable property. In general, optimal order of accuracy is recovered. Suboptimal accuracy is observed for the coarser resolutions with $p = 1$, likely because the asymptotic regime is not yet reached.

Fig. 8.2 compares the temperature and pressure profiles at $t = 50$ s computed with the local entropy bound in [17] (“Old EB”) to that computed with the local entropy bound in Equation (5.20) (“New EB”). The exact solution is the same as the initial condition. The element size is $h/4$, and $p = 1$ and $p = 2$ solutions are computed. For $p = 1$, though oscillations in temperature are present with both types of entropy bounds, they are significantly larger with the local entropy bound in [17]. The more aggressive limiting increases inter-element jumps and causes larger deviations from pressure equilibrium, suggesting that this entropy bound may be too disruptive. Also displayed in Fig. 8.2 is the solution computed with only the positivity-preserving limiter, which yields slightly smaller deviations from pressure equilibrium than the proposed local entropy limiter but noticeably larger oscillations in temperature. Recall that the modified flux interpolation (3.9) maintains pressure equilibrium in an approximate sense [14,112]; deviations from pressure equilibrium may still occur if the solution is not fully resolved, but they remain small over long times. In contrast, with standard flux interpolation, spurious pressure oscillations grow rapidly, which can cause solver divergence. For $p = 2$, the entropy limiter with the bound in Equation (5.20) is not activated. However, with the bound in [17], the entropy limiter is clearly overly aggressive, causing large errors in temperature, although it should be noted that the minimum entropy is not calculated exactly when computing the entropy bounds for $p = 2$. Conversely, for $p = 1$, the minimum entropy is indeed calculated exactly (see Section 5.2.3). The local Lax-Friedrichs flux is employed in these comparisons. With the selected parameters, the differences between the two local entropy bounds are more pronounced for this numerical flux than the HLLC flux. Nevertheless, such discrepancies are observed for the latter flux function in other configurations as well.

For a more detailed assessment of the effects of increasing polynomial order, Fig. 8.3 compares $p = 1$, $p = 2$, and $p = 3$ solutions at $t = 50$ s obtained with the HLLC flux function, an element size of $h/2$, and the proposed local entropy limiter. Profiles of temperature, pressure, velocity, and specific thermodynamic entropy are shown. Increasing the polynomial order yields better predictions in the temperature and entropy profiles and smaller deviations from pressure and velocity equilibrium.

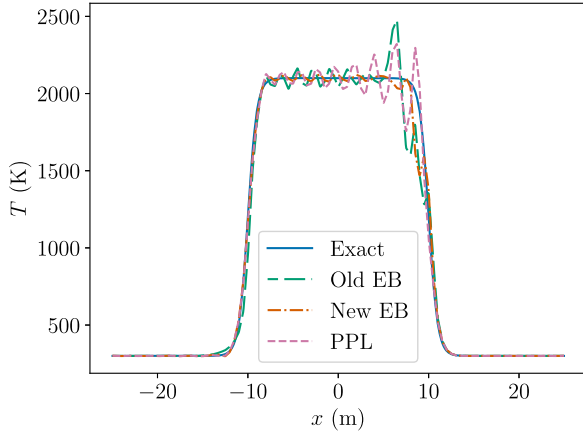
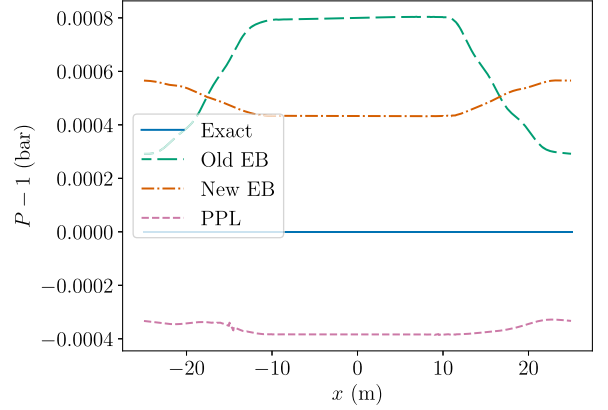
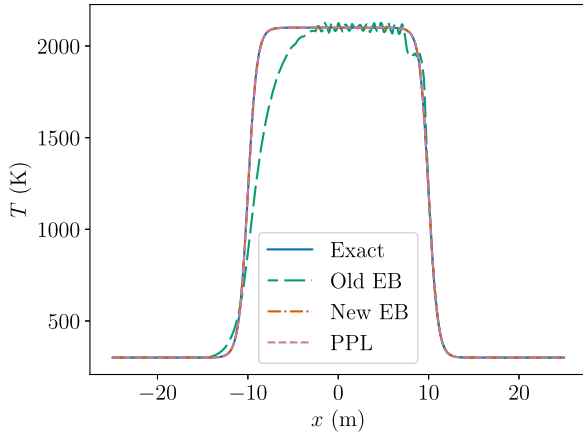
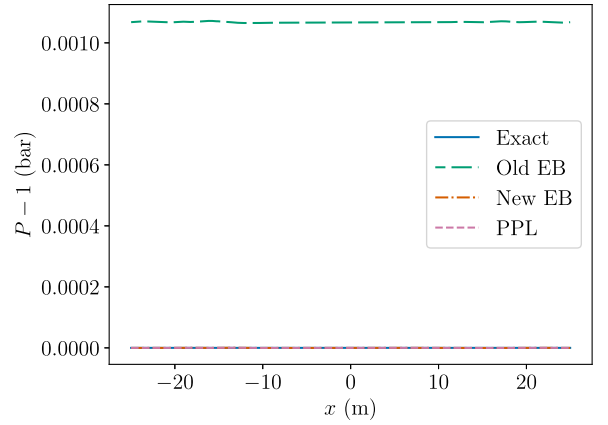
(a) $p = 1$, temperature.(b) $p = 1$, pressure.(c) $p = 2$, temperature.(d) $p = 2$, pressure.

Fig. 8.2. Temperature and pressure profiles at $t = 50$ s computed with the local entropy bound in [17] (“Old EB”), the local entropy bound in Equation (5.20) (“New EB”), and the positivity-preserving limiter only. The exact solution is the same as the initial condition. The element size is $h/4$, and the polynomial orders are $p = 1$ and $p = 2$.

8.2. Low-density Gaussian wave

To further assess the grid convergence of the proposed formulation, we consider the advection of a multicomponent, low-density Gaussian wave, as introduced by Trojak and Dzanic [97]. A periodic domain $\Omega = [-0.5, 0.5]$ m is initialized in nondimensional form as follows:

$$\begin{aligned}
 v &= 1, \\
 Y_1 &= \frac{1}{2} [\sin(2\pi x) + 1], \\
 Y_2 &= 1 - Y_1, \\
 \rho &= \exp(-\sigma x^2) + 4\epsilon, \\
 P &= 2\epsilon,
 \end{aligned} \tag{8.2}$$

where $\sigma = 500$ and $\epsilon = 10^{-12}$, yielding near-vacuum conditions that encourage activation of the limiting procedure. The thermodynamic relations for the two fictitious species considered here are written as

$$\begin{aligned}
 \frac{W_1 c_{p,1}(T)}{R^0} &= 3.5, & \frac{W_1 h_1(T)}{R^0} &= 3.5 T_r \hat{T}, & \frac{W_1 s_1^0}{R^0} &= 3.5 \ln \hat{T}, \\
 \frac{W_2 c_{p,2}(T)}{R^0} &= 2.491, & \frac{W_2 h_2(T)}{R^0} &= 2.491 T_r \hat{T}, & \frac{W_2 s_2^0}{R^0} &= 2.491 \ln \hat{T}.
 \end{aligned}$$

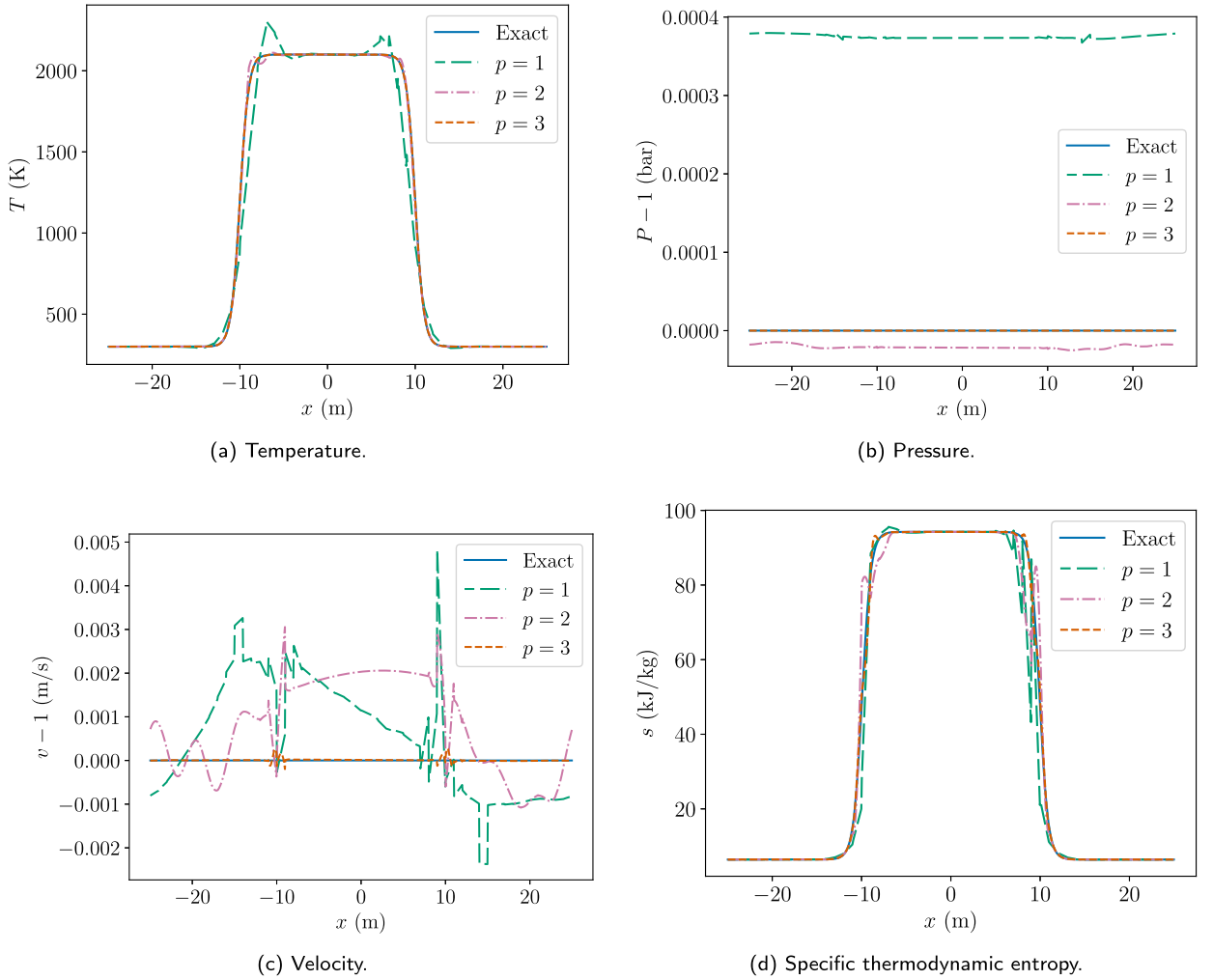


Fig. 8.3. Temperature, pressure, velocity, and entropy profiles at $t = 50$ s computed with the proposed local entropy limiter and an element size of $h/2$. $p = 1$, $p = 2$, and $p = 3$ solutions are computed. The exact solution is the same as the initial condition.

Five element sizes are considered: h , $h/2$, $h/4$, $h/8$, and $h/16$, where $h = 0.04$. The solution is integrated in time using the SSPRK3 time stepping scheme since the SSPRK2 method with $\text{CFL} = 0.1$ fails to maintain sufficiently low temporal errors. The L^2 error at $t = 1$, corresponding to one advection period, is calculated in terms of the normalized state variables, as in the previous test case. Fig. 8.4 presents the results of the convergence study for $p = 1$ to $p = 3$, where again, the “x” marker indicates that the positivity-preserving limiter is activated and the “o” marker indicates that the entropy limiter is activated. The dashed lines represent the theoretical convergence rates. The entropy limiter is activated for the coarser cases, while the positivity-preserving limiter is activated for all cases. High-order accuracy is observed.

8.3. Shock tube

This test case was first presented by Houim and Kuo [113] and computed as well by Johnson and Kercher [14]. The goals here are to compare the stabilization properties of the limiters and to illustrate the benefits of the local entropy bound. The initial conditions are given by

$$\left(v_1, T, P, Y_{N_2}, Y_{He} \right) = \begin{cases} (0 \text{ m/s}, 300 \text{ K}, 1 \text{ atm}, 1, 0), & x \geq 0.4 \\ (0 \text{ m/s}, 300 \text{ K}, 10 \text{ atm}, 0, 1), & x < 0.4 \end{cases} \quad (8.3)$$

The thermodynamic relations for the considered nitrogen-helium mixture are written as

$$\frac{W_{N_2} c_{p,N_2}(T)}{R^0} = 3.20 + 0.926\hat{T} - 0.212\hat{T}^2 + 0.0117\hat{T}^3 + 0.000938\hat{T}^4,$$

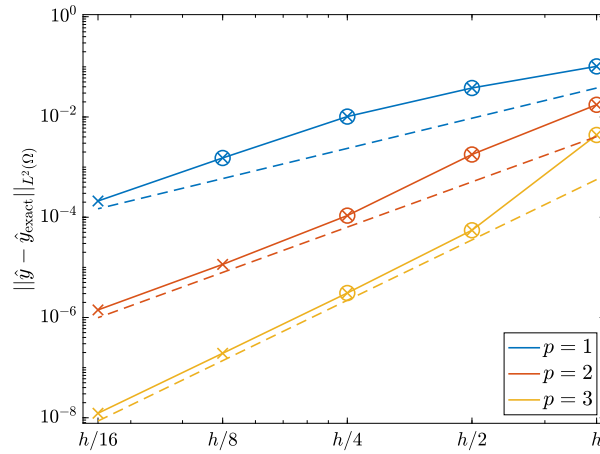


Fig. 8.4. Convergence under grid refinement, with $h = 0.04$, for the low-density Gaussian-wave test. The L^2 error of the normalized state with respect to the exact solution at $t = 1$ is computed. The dashed lines represent the theoretical convergence rates. The “x” marker indicates that the positivity-preserving limiter is activated, and the “o” marker indicates that the entropy limiter is activated. If both limiters are activated, then the corresponding markers are superimposed as “⊗”.

$$\begin{aligned} \frac{W_{N_2} h_{N_2}(T)}{R^0} &= \int \frac{W_{N_2} c_{p,N_2}(\tau) d\tau}{R^0} - 994.7 \text{ K}, & \frac{W_{N_2} s_{N_2}^0}{R^0} &= \int \frac{W_{N_2} c_{p,N_2}(\tau) d\tau}{R^0 \tau} + 4.52, \\ \frac{W_{He} c_{p,He}(T)}{R^0} &= 2.50, \\ \frac{W_{He} h_{He}(T)}{R^0} &= \int \frac{W_{He} c_{p,He}(\tau) d\tau}{R^0} - 745.4 \text{ K}, & \frac{W_{He} s_{He}^0}{R^0} &= \int \frac{W_{He} c_{p,He}(\tau) d\tau}{R^0 \tau} + 0.929. \end{aligned}$$

The computational domain is $\Omega = [0, 1]$ m, with walls at both ends. Fig. 8.5 shows the mass fraction, pressure, temperature, and entropy profiles at $t = 300 \mu\text{s}$ for $p = 3$ and 200 elements. We present results for only the positivity-preserving limiter (referred to as “PPL”) and for both the positivity-preserving and entropy limiters with the local entropy bound in Equation (5.20) (referred to as “local EB”). Also included is a reference solution computed with $p = 2$, 2000 elements, and artificial viscosity, which corresponds to the configuration in [14]. Artificial viscosity is not employed in the coarser cases in order to isolate the effects of the limiters. The mass fraction profiles are well-captured for both types of limiting. However, although the solver does not crash, the positivity-preserving limiter by itself fails to suppress large-scale oscillations and significant overshoots/undershoots in the pressure and temperature distributions. While instabilities are still present with the local entropy limiter, they are of substantially smaller magnitude. The entropy distribution obtained with the local entropy limiter is very similar to that of the reference solution, whereas the positivity-preserving limiter generates a notable overshoot and undershoot at the shock. For the given flow conditions, the global entropy bound yields very similar results (not shown for brevity) to the local entropy bound since the specific thermodynamic entropy in the vicinity of the shock, which is where much of the limiting occurs, is close to the global minimum. It should also be noted that although the entropy limiter appreciably reduces the magnitude of nonphysical oscillations in the pressure field, Gouasmi et al. [51] found that the deviations from pressure equilibrium intrinsic to multicomponent-flow simulations using fully conservative schemes are not tied to violations of the minimum entropy principle.

The instabilities observed in the “PPL” case in Figs. 8.5b and 8.5c are considerably larger than those typically observed in shock-tube solutions obtained with the positivity-preserving limiter in the monocomponent, calorically perfect case [20,36,35]. This difference reflects the numerical challenges associated with not only multicomponent mixtures, but also variable thermodynamics. In a similar vein, the relative benefit of the entropy limiter (compared to the positivity-preserving limiter) seems significantly greater in the multicomponent, thermally perfect case than in the monocomponent, calorically perfect case.

Fig. 8.6 presents the percent error in conservation of mass, energy, and atomic elements for the “local EB” case as a representative example, calculated every $0.3 \mu\text{s}$ (for a total of 1000 samples). N_N and N_{He} denote the total moles of nitrogen and helium in the mixture, computed as

$$N_N = \int_{\Omega} 2C_N dx, \quad N_{He} = \int_{\Omega} C_{He} dx.$$

The error remains close to machine precision, confirming that the proposed formulation is conservative. Also included is the error in mass conservation (calculated every time step) for a solution computed without the positivity-preserving and entropy limiters, but instead with a simple clipping procedure in which negative species concentrations are set to zero, a strategy employed by many reacting-flow solvers. The error increases rapidly to non-negligible values until the solver diverges.

Next, we recompute this problem with artificial viscosity to confirm adequate suppression of small-scale oscillations. Fig. 8.7 presents the results for $C_{AV} = 1$. The instabilities observed in Fig. 8.5 are largely eliminated by the artificial viscosity. As shown in Fig. 8.7c, a temperature undershoot at the shock emerges when only the positivity-preserving limiter is used, but is suppressed by the

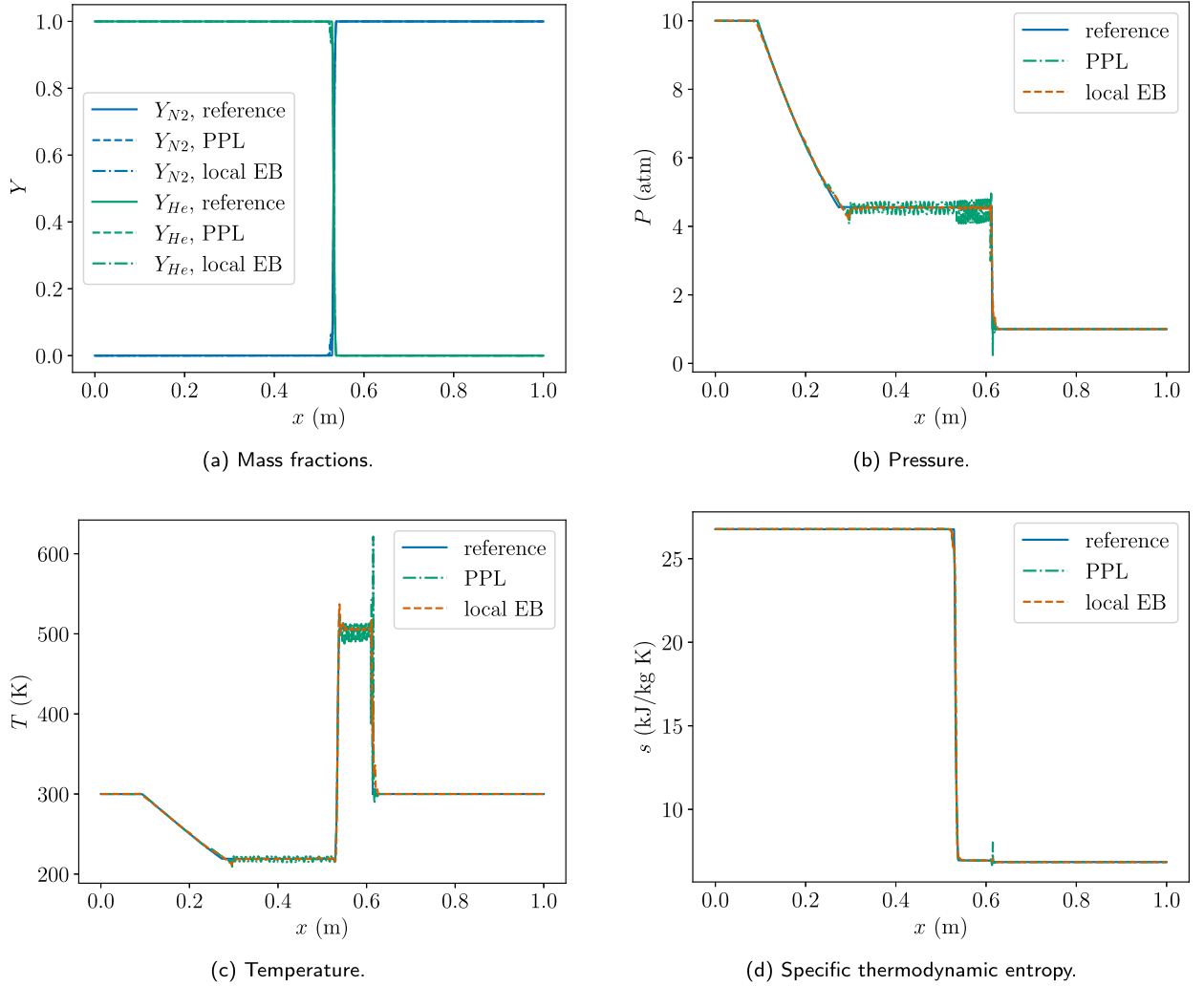


Fig. 8.5. Results for $p = 3$ solutions on 200 elements without artificial viscosity for the one-dimensional, multicomponent shock-tube problem with initialization in Equation (8.3). “PPL” corresponds to the positivity-preserving limiter by itself, and “local EB” refers to both the positivity-preserving and entropy limiters with the local entropy bound in Equation (5.20). The reference solution [14] is computed with $p = 2$, 2000 elements, and artificial viscosity.

entropy limiter. The artificial viscosity causes slight smearing of the solution at the contact, but spurious pressure oscillations typically associated with fully conservative schemes in multicomponent-flow simulations are suppressed. Note that without any limiting, negative species concentrations occur for the $p = 3$, 200-element cases, even with artificial viscosity. As will be further discussed in Part II [19], artificial viscosity alone, or even when combined with solely the positivity-preserving limiter, may not provide sufficient stabilization in simulations of complex detonation waves on relatively coarse meshes. In these simulations, enforcement of the entropy principle is critical for robustness.

To highlight discrepancies between the local and global entropy bounds, we consider different initial conditions, given by

$$\left(v_1, T, P, Y_{N_2}, Y_{He} \right) = \begin{cases} (0 \text{ m/s}, 300 \text{ K}, 1 \text{ atm}, 0, 1), & x \geq 0.4 \\ (0 \text{ m/s}, 300 \text{ K}, 10 \text{ atm}, 1, 0), & x < 0.4 \end{cases}. \quad (8.4)$$

The only difference with the previous initial conditions is in the mass fractions. Displayed in Fig. 8.8 are the results obtained with the global entropy bound (referred to as “global EB”) and the local entropy bound (again referred to as “local EB”). These $p = 2$ solutions are computed on 200 elements without any artificial viscosity. The positivity-preserving limiter by itself yields very similar results (not shown for brevity) to the entropy limiter with the global entropy bound. The reference solution is again computed with $p = 2$, 2000 elements, and artificial viscosity. The mass fractions are well-captured in all cases. The differences between the “global EB” and “local EB” solutions here are not as large as those between the “PPL” and “local EB” solutions in Fig. 8.5. Nevertheless, the benefit of the local entropy bound is evident, specifically at the shock. Spurious artifacts in the pressure profile and especially the temperature profile near the shock are noticeably larger for the global entropy bound. The discrepancies between the two solutions are attributed to the considerable difference between the specific thermodynamic entropy in the vicinity of the shock and the global minimum,

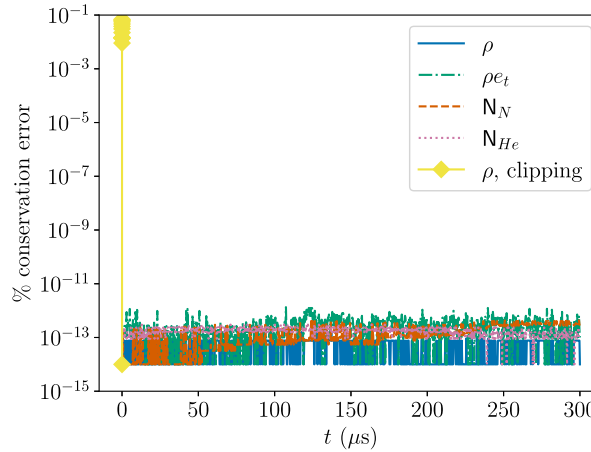


Fig. 8.6. Percent error in conservation of mass, energy, and atomic elements for the “local EB” case in Fig. 8.5, computed with $p = 3$ on 200 elements. The initial conditions for this one-dimensional, multicomponent shock-tube problem are given in Equation (8.3). Also included is the error in mass conservation for a solution computed without the positivity-preserving and entropy limiters, but instead with a simple clipping procedure in which negative species concentrations are set to zero.

as illustrated in Fig. 8.8d. As such, the local entropy bound is particularly beneficial in flow problems with large variations in the specific thermodynamic entropy throughout the domain.

8.4. Detonation wave

The final one-dimensional test case is a hydrogen-oxygen detonation wave diluted in Argon with initial conditions

$$\begin{aligned}
 v_1 &= 0 \text{ m/s,} \\
 X_{Ar} : X_{O_2} : X_{H_2} &= 7 : 1 : 2 & x > 0.025 \text{ m,} \\
 X_{Ar} : X_{O_2} : X_{H_2} : X_{OH} &= 7 : 1 : 2 : 0.01 & 0.015 \text{ m} < x < 0.025 \text{ m,} \\
 X_{Ar} : X_{H_2O} : X_{OH} &= 8 : 2 : 0.0001 & x < 0.015 \text{ m,} \\
 P &= \begin{cases} 5.50\text{e5} & \text{Pa} & x < 0.015 \text{ m} \\ 6.67\text{e3} & \text{Pa} & x > 0.015 \text{ m} \end{cases}, \\
 T &= \begin{cases} 298 & \text{K} & x > 0.025 \text{ m} \\ 350 & \text{K} & 0.015 \text{ m} < x < 0.025 \text{ m} . \\ 3500 & \text{K} & x < 0.015 \text{ m} \end{cases}.
 \end{aligned} \tag{8.5}$$

We consider a chemical mechanism obtained by extracting all thermodynamic relations and chemical reactions involving the following species from the well-known GRI-3.0 mechanism [114]: $H_2, H, O, O_2, OH, H_2O, HO_2, H_2O_2, N_2, Ar$. The domain is $\Omega = (0, 0.45) \text{ m}$, with walls at the left and right boundaries. In previous work [14], this case was computed with $p = 1$ and mesh spacing $h = 9 \times 10^{-5} \text{ m}$. At this resolution, artificial viscosity was the only stabilization necessary to obtain an accurate solution while maintaining conservation of mass and energy. Good agreement with the Shock and Detonation Toolbox [115] was observed. Additional details can be found in [14]. Here, our objective is to demonstrate that the developed formulation can compute stable and accurate solutions with appreciably lower resolution. In light of [14], we use a $p = 1, h = 9 \times 10^{-5}$ calculation as a reference solution. Note that the reaction mechanism employed in this study is different from that in [14].

Fig. 8.9 presents $p = 1, p = 2$, and $p = 3$ results at $t = 235 \mu\text{s}$ computed with entropy-stable DGODE alone. The mesh spacing in these simulations is $h = 4.5 \times 10^{-4} \text{ m}$, which is five times larger than for the reference solution. Artificial viscosity and the local entropy limiter are employed. At this mesh spacing, artificial viscosity alone is not sufficient to stabilize the solution. Good agreement in temperature and pressure with the reference solution is observed. As shown in Fig. 8.9b, which zooms in on the shock, there are slight discrepancies in the predictions of the leading-shock-front location, especially for $p = 1$ and $p = 2$. We also compute a $p = 1$ solution with the mean-value numerical state function (6.15) to ensure that entropy-stable DGODE is not the primary cause of disagreement. As illustrated in Fig. 8.9b, the two $p = 1$ solutions are extremely similar. Fig. 8.9d shows small-scale entropy oscillations behind the leading shock front, which are reduced for the higher polynomial orders.

Additional diagnostics are obtained for the $p = 1$ calculations as a representative example. Fig. 8.10a presents the temporal variation of the global minimum of specific thermodynamic entropy, which remains relatively constant at the entropy of the unburnt gas. The small oscillations are a result of numerical-precision issues associated primarily with the entropy limiter. As reported in [96,97], due to the logarithm operation in Equation (2.5), the entropy is more prone to such issues than other variables. Fig. 8.10b displays the variation of the time-step size every 100 steps. At start-up, the time-step size is highest and quickly decreases as high-temperature chemical reactions occur, eventually reaching a steady value. The results presented in Fig. 8.10 are very similar between

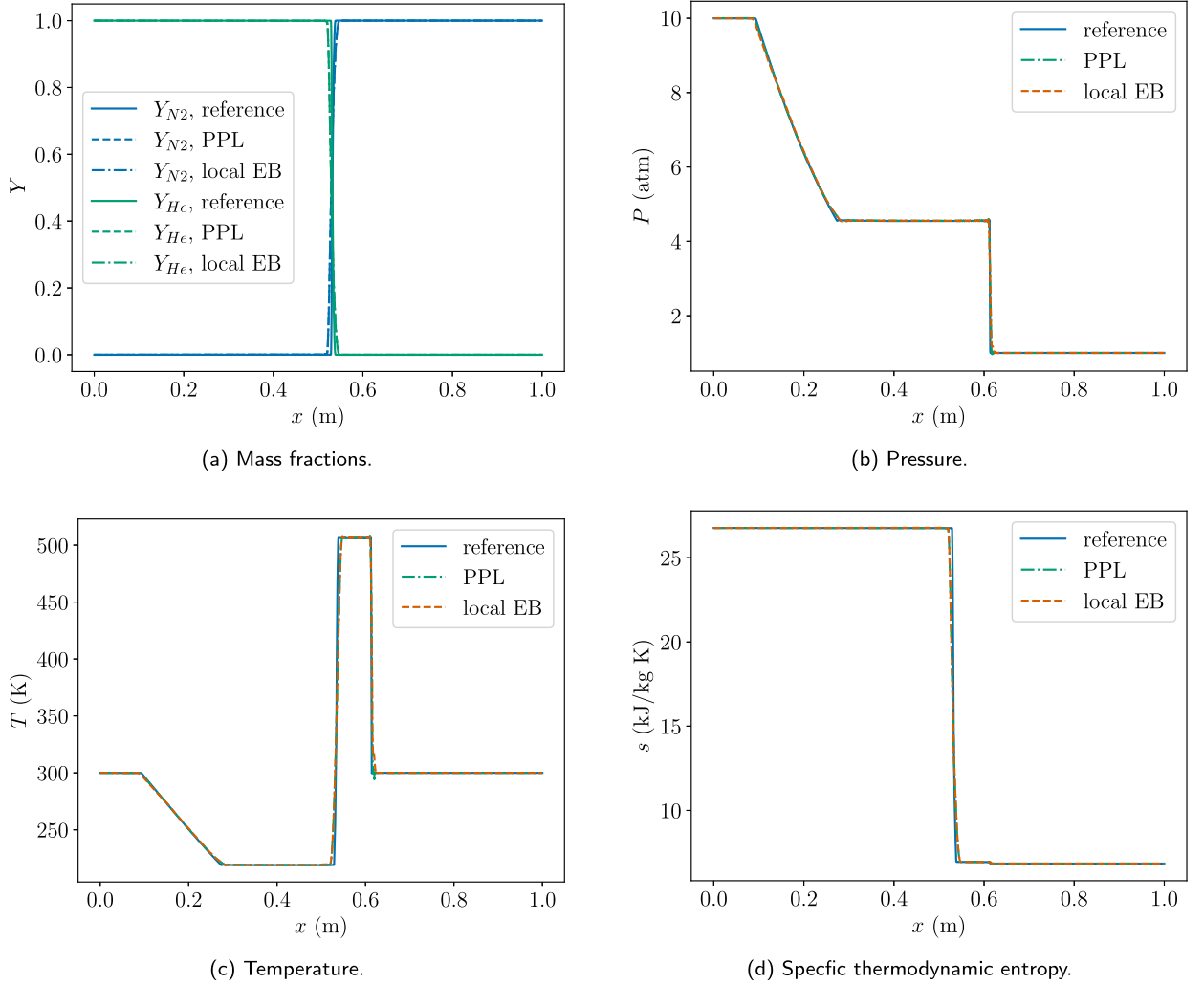


Fig. 8.7. Results for $p = 3$ solutions on 200 elements with artificial viscosity for the one-dimensional, multicomponent shock-tube problem with initialization in Equation (8.3). “PPL” corresponds to the positivity-preserving limiter by itself, and “local EB” refers to both the positivity-preserving and entropy limiters with the local entropy bound in Equation (5.20). The reference solution [14] is computed with $p = 2$, 2000 elements, and artificial viscosity. The difference between these results and those in Fig. 8.5 is the use of artificial viscosity in the (non-reference) solutions here.

the solutions. However, the computational cost of entropy-stable DGODE is noticeably higher, motivating the solution procedure recommended in Remark 7. At the first step of the calculation, using the mean-value numerical state (6.15), the global maximum number of DGODE sub-time-steps taken is four (which occurs in the high-temperature region). Recall that a sub-time-step refers to a “cell” as described in Section 6.1. In contrast, with entropy-stable DGODE, the global maximum is 68 sub-time-steps, and the computational cost is approximately 16 times higher. The number of sub-time-steps in the remainder of both calculations is one, in which case entropy-stable DGODE is almost twice as expensive.

Finally, Fig. 8.11 gives the percent error in conservation of mass, energy, and atomic elements for $p = 1$, calculated every $0.235 \mu\text{s}$ (for a total of 1000 samples). N_O , N_H , and N_{Ar} denote the total moles of oxygen, hydrogen, and argon atoms in the mixture, computed as

$$\begin{aligned}
 N_O &= \int_{\Omega} \left(C_O + 2C_{O_2} + C_{OH} + C_{H_2O} + 2C_{HO_2} + 2C_{H_2O_2} \right) dx, \\
 N_H &= \int_{\Omega} \left(2C_{H_2} + C_H + C_{OH} + 2C_{H_2O} + C_{HO_2} + 2C_{H_2O_2} \right) dx, \\
 N_{Ar} &= \int_{\Omega} C_{Ar} dx.
 \end{aligned}$$

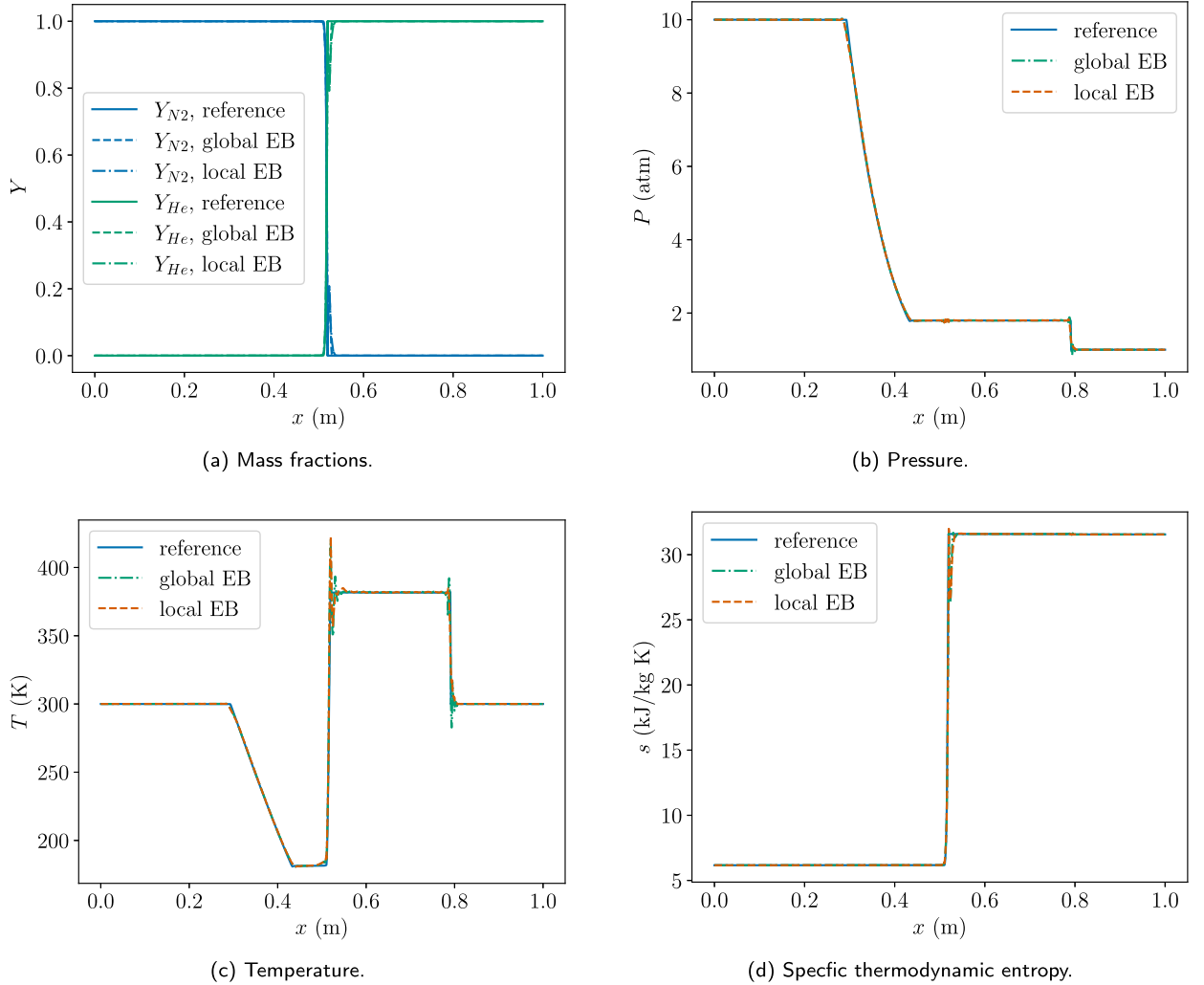


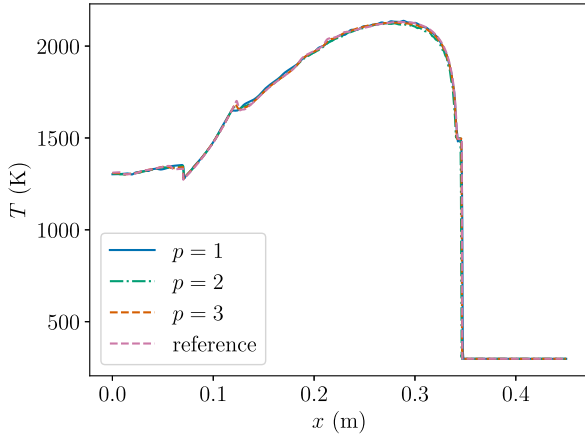
Fig. 8.8. Results for $p = 2$ solutions on 200 elements without artificial viscosity for the one-dimensional, multicomponent shock-tube problem with initialization in Equation (8.4). “Global EB” refers to the entropy limiter with the global entropy bound in Equation (5.15), and “local EB” refers to the entropy limiter with the local entropy bound in Equation (5.20). The reference solution is computed with $p = 2$, 2000 elements, and artificial viscosity.

The error remains negligible throughout the simulation, confirming that the methodology is conservative.

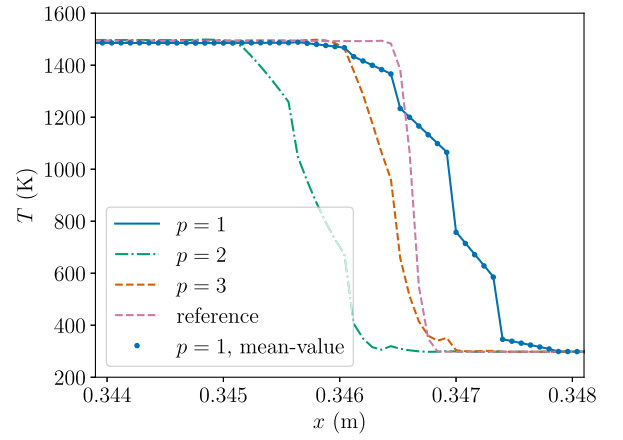
9. Concluding remarks

In this paper, we introduced a positivity-preserving and entropy-bounded DG methodology for the chemically reacting, compressible Euler equations. The methodology builds on the fully conservative, high-order DG method previously introduced in [14], which does not generate spurious pressure oscillations in smooth flow regions or across material interfaces when the temperature is continuous. As a prerequisite for the proposed formulation, we proved a minimum entropy principle for the compressible, multicomponent, chemically reacting Euler equations, which follows from the proof by Gouasmi et al. [16] of a minimum entropy principle for the compressible, multicomponent, nonreacting Euler equations.

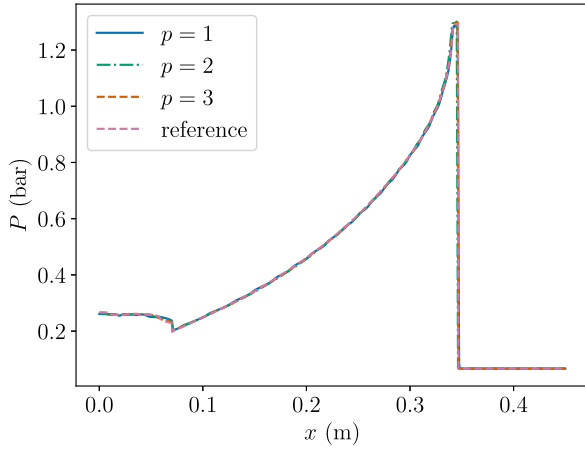
In this first part of our two-part paper, we focused on the one-dimensional case. A simple linear-scaling limiter ensures that the solution at a given time step is admissible (i.e., species concentrations are nonnegative, density is positive, pressure is positive, and entropy is greater than some lower bound). A requirement of the limiter is that the element average of the state is itself admissible, which we showed to be true under the following conditions: (a) a time-step-size constraint is satisfied, (b) an invariant-region-preserving numerical flux is employed, and (c) certain pointwise values of the solution at the previous time step are admissible. Both a global entropy bound and a local entropy bound were discussed. Since the linear scaling does not completely eliminate small-scale oscillations, artificial viscosity is employed in tandem. We also detailed how to maintain compatibility between the proposed framework and the pressure-equilibrium-maintaining discretization in [14]. The temporal integration of the convection operator is decoupled from that of the stiff chemical source term via Strang splitting. To guarantee satisfaction of the minimum entropy principle



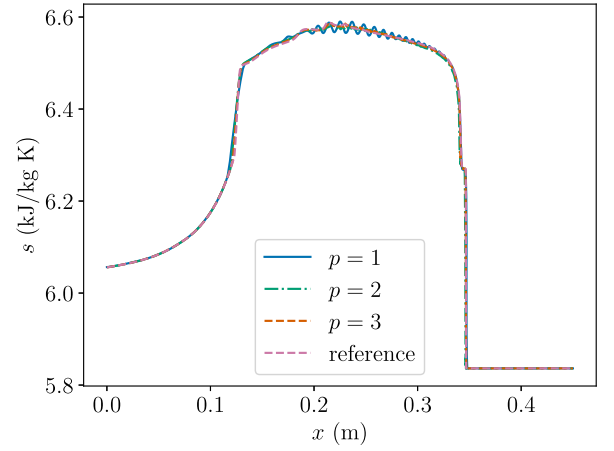
(a) Temperature.



(b) Temperature, zoomed in on detonation front.

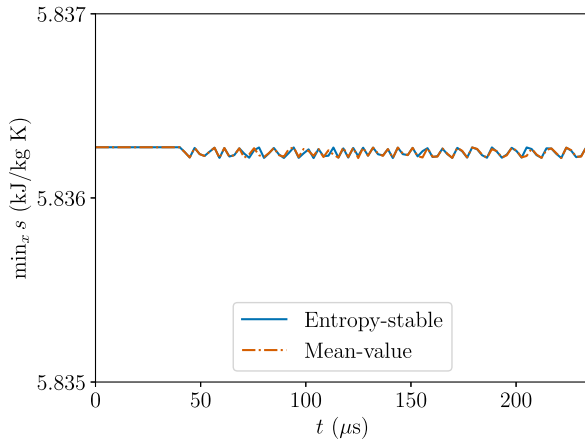


(c) Pressure.

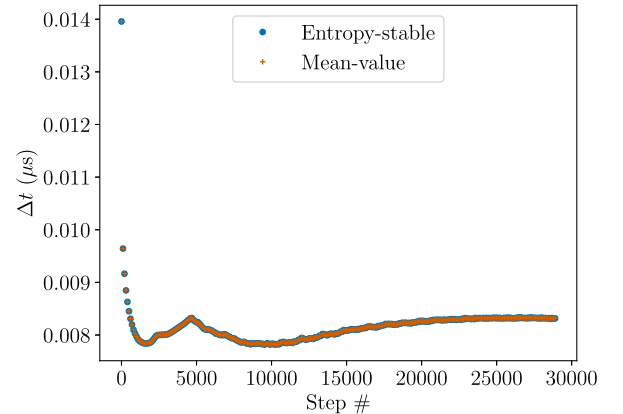


(d) Specific thermodynamic entropy.

Fig. 8.9. $p = 1$, $p = 2$, and $p = 3$ results at $t = 235 \mu\text{s}$ for the one-dimensional hydrogen detonation test case. The mesh spacing in these simulations is $h = 4.5 \times 10^{-4}$ m, which is five times larger than for the reference solution. Artificial viscosity and the local entropy limiter are employed.



(a) Temporal variation of global minimum of entropy .



(b) Variation of time-step size.

Fig. 8.10. Temporal variation of global minimum of entropy and variation of time-step size for the $p = 1$ calculations. The initial conditions for this one-dimensional hydrogen detonation problem are given in Equation (8.5).

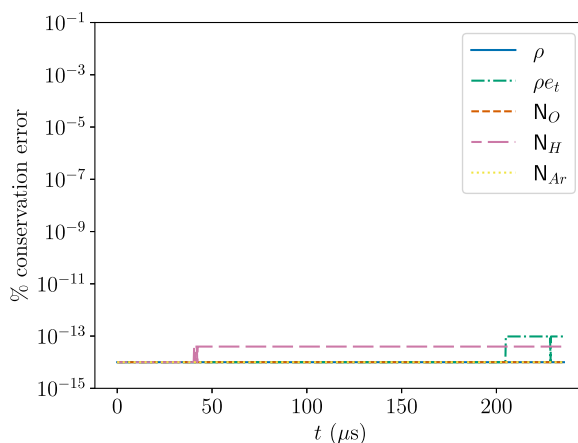


Fig. 8.11. Percent error in conservation of mass, energy, and atomic elements for $p = 1$ with $h = 4.5 \times 10^{-4}$ m. The initial conditions for this one-dimensional hydrogen detonation problem are given in Equation (8.5).

in the reaction step, we developed an entropy-stable discontinuous Galerkin method based on diagonal-norm summation-by-parts operators for temporal integration of the source term, which involved the derivation of an entropy-conservative two-point numerical state function.

The methodology was applied to canonical one-dimensional test cases. The first three entailed nonreacting flows: advection of a smooth, hydrogen-oxygen thermal bubble, advection of a low-density Gaussian wave, and nitrogen-helium shock-tube flow. In the first one, we demonstrated sufficient preservation of pressure equilibrium. Optimal convergence of the methodology was observed in the first and second configurations. In the third test, we observed the following:

- The positivity-preserving limiter (which does not consider an entropy bound) prevents the solver from crashing, but, in the absence of additional stabilization, gives rise to large-scale oscillations. Such instabilities are substantially larger than those typically seen in the monocomponent, calorically perfect case, illustrating the challenges of stabilizing computations of multi-component flows with realistic thermodynamics.
- The entropy limiter, on the other hand, considerably reduces the magnitude of the aforementioned instabilities, suggesting that the relative benefit of the entropy limiter is much greater in the multicomponent, thermally perfect case. Small-scale oscillations are still present, but these can be cured with artificial viscosity. Note that the inability to completely eliminate oscillations is a well-known property of the linear-scaling limiter [20,35,17]. Furthermore, unless a very fine resolution is employed, artificial viscosity alone is insufficient for robustness.
- Enforcing a local entropy bound can be more effective than enforcing a global entropy bound when the entropy varies significantly throughout the domain.

In our final test case, we computed a moving hydrogen-oxygen detonation wave diluted in Argon, demonstrating that the developed methodology can accurately and robustly calculate a chemically reacting flow with detailed chemistry using high-order polynomial approximations on relatively coarse meshes. Conservation of mass, total energy, and atomic elements was confirmed.

In Part II [19], we will extend our formulation to multiple dimensions. In our developed multidimensional framework, restrictions on the physical modeling, geometry, numerical flux function, and quadrature rules are milder than those currently in the literature. Complex two- and three-dimensional detonations will be accurately computed in a stable manner using high-order polynomial approximations.

CRediT authorship contribution statement

Eric J. Ching: Conceptualization, Investigation, Methodology, Software, Writing – original draft. **Ryan F. Johnson:** Conceptualization, Investigation, Methodology, Software, Writing – review & editing. **Andrew D. Kercher:** Conceptualization, Methodology, Software, Writing – review & editing.

Declaration of competing interest

The authors declare that they have no known competing financial interests or personal relationships that could have appeared to influence the work reported in this paper.

Data availability

Data will be made available on request.

Acknowledgements

The authors wish to acknowledge Dr. Eric Marineau of the Hypersonic Aerothermodynamics, High-Speed Propulsion and Materials Program of ONR Code 35 for directly supporting this work.

Appendix A. Concavity of shifted internal energy

Lemma 9. The “shifted” internal energy per unit volume,

$$\rho u^* = \rho u - \sum_{i=1}^{n_s} \rho_i b_{i0}, \quad (\text{A.1})$$

is a concave function of the state for $\rho > 0$.

Proof. Throughout this proof, we work with $d = 3$ and, without loss of generality, a re-ordered state vector where the species concentrations are replaced by the partial densities:

$$y = \left(\rho v_1, \dots, \rho v_d, \rho_1, \dots, \rho_{n_s}, \rho e_t \right)^T.$$

It is well-known that a function is concave if and only if its Hessian is negative semidefinite. Here, $\mathcal{H} = \frac{d^2(\rho u^*)}{dy^2}$ denotes the Hessian of ρu^* , which is a symmetric matrix of size m . We observe that since the second term on the RHS of Equation (A.1) is linear with respect to the state, $\frac{d^2}{dy^2} \left(\sum_{i=1}^{n_s} \rho_i b_{i0} \right)$ gives a matrix of zeros; thus, $\mathcal{H} = \frac{d^2(\rho u)}{dy^2}$. There exist various ways to show negative semidefiniteness. One approach is to check the signs of the principal minors [116,117], where an l -th-order principal minor, \mathcal{M}_l , of \mathcal{H} is the determinant of a submatrix obtained by eliminating $m-l$ rows and the corresponding $m-l$ columns from \mathcal{H} . Specifically, \mathcal{H} is negative semidefinite if and only if all even-order principal minors are nonnegative and all odd-order principal minors are nonpositive.

We start with some useful relations:

$$\begin{aligned} \frac{\partial^2(\rho u)}{\partial(\rho v_k) \partial(\rho v_k)} &= -\frac{1}{\rho}, \\ \frac{\partial^2(\rho u)}{\partial(\rho v_k) \partial(\rho v_l)} &= 0, \quad k \neq l, \\ \frac{\partial^2(\rho u)}{\partial \rho_i \partial \rho_j} &= -\frac{|v|^2}{\rho}, \\ \frac{\partial^2(\rho u)}{\partial \rho_i \partial(\rho v_k)} &= \frac{v_k}{\rho}, \\ \frac{\partial^2(\rho u)}{\partial \rho_i \partial(\rho e_t)} &= \frac{\partial^2(\rho u)}{\partial(\rho v_k) \partial(\rho e_t)} = \frac{\partial^2(\rho u)}{\partial(\rho e_t) \partial(\rho e_t)} = 0. \end{aligned}$$

\mathcal{H} can then be written as

$$\mathcal{H} = \begin{pmatrix} -\frac{1}{\rho} & 0 & 0 & \frac{v_1}{\rho} & \dots & \frac{v_1}{\rho} & 0 \\ 0 & -\frac{1}{\rho} & 0 & \frac{v_2}{\rho} & \dots & \frac{v_2}{\rho} & \vdots \\ 0 & 0 & -\frac{1}{\rho} & \frac{v_3}{\rho} & \dots & \frac{v_3}{\rho} & 0 \\ \frac{v_1}{\rho} & \frac{v_2}{\rho} & \frac{v_3}{\rho} & -\frac{|v|^2}{\rho} & \dots & -\frac{|v|^2}{\rho} & 0 \\ \vdots & \vdots & \vdots & \vdots & \ddots & \vdots & \vdots \\ \frac{v_1}{\rho} & \frac{v_2}{\rho} & \frac{v_3}{\rho} & -\frac{|v|^2}{\rho} & \dots & -\frac{|v|^2}{\rho} & 0 \\ 0 & \dots & 0 & 0 & \dots & 0 & 0 \end{pmatrix}. \quad (\text{A.2})$$

The m first-order principal minors, \mathcal{M}_1 , are simply the diagonal entries, which are all nonpositive. The principal minors of order greater than one take the following forms:

$$\mathcal{M}_l^0 = \det \begin{pmatrix} a_{1,1} & \dots & a_{1,l-1} & 0 \\ \vdots & \ddots & \vdots & \vdots \\ a_{l-1,1} & \dots & a_{l-1,l-1} & \vdots \\ 0 & \dots & \dots & 0 \end{pmatrix}, \quad l = 2, \dots, m, \quad (\text{A.3})$$

$$\mathcal{M}_l^1 = \det \begin{pmatrix} -\frac{1}{\rho} & 0 & 0 \\ 0 & \ddots & 0 \\ 0 & 0 & -\frac{1}{\rho} \end{pmatrix}, \quad l = 2, \dots, d, \quad (\text{A.4})$$

$$\mathcal{M}_l^2 = \det(B_l), B_l = \begin{pmatrix} -\frac{|v|^2}{\rho} & \dots & -\frac{|v|^2}{\rho} \\ \vdots & \ddots & \vdots \\ -\frac{|v|^2}{\rho} & \dots & -\frac{|v|^2}{\rho} \end{pmatrix}, l = 2, \dots, n_s, \quad (\text{A.5})$$

$$\begin{aligned} \mathcal{M}_l^3 &= \det(C_l) = \det \left(\begin{array}{c|c} C_{1,1} & C_{1,2} \\ \hline C_{2,1} & B_q \end{array} \right) \\ &= \det \left(\begin{array}{c|c} C_{1,1} & C_{1,2} \\ \hline C_{2,1} & \begin{array}{ccc} -\frac{|v|^2}{\rho} & \dots & -\frac{|v|^2}{\rho} \\ \vdots & \ddots & \vdots \\ -\frac{|v|^2}{\rho} & \dots & -\frac{|v|^2}{\rho} \end{array} \end{array} \right), q = 1, \dots, n_s; l = q + 1, \dots, q + d. \end{aligned} \quad (\text{A.6})$$

\mathcal{M}_l^0 is zero due to the row of zeros (note that the m th-order principal minor, $\mathcal{M}_m = \det(\mathcal{H})$, takes this form); \mathcal{M}_l^1 is negative for l odd and positive for l even; and \mathcal{M}_l^2 is zero due to linear dependence of the rows. For \mathcal{M}_l^3 , the corresponding submatrix, C_l , is written in block-matrix form, where the lower-right block is a matrix of size q of the form in Equation (A.5). We consider two cases: $q = 1$ and $q \geq 1$. In the latter case, $\mathcal{M}_l^3 = 0$ since the last q rows of C_l are repeated. In the former, we first consider $l = 2$, which yields

$$\mathcal{M}_2^3 = \det \begin{pmatrix} -\frac{1}{\rho} & \frac{v_k}{\rho} \\ \frac{v_k}{\rho} & -\frac{|v|^2}{\rho} \end{pmatrix} = \frac{|v|^2}{\rho^2} - \frac{v_k^2}{\rho^2}, k = 1, \dots, d,$$

which is nonnegative since $|v|^2 = \sum_i v_i^2 \geq v_k^2 \geq 0$. For $l = 3$, we have

$$\mathcal{M}_4^3 = \det \begin{pmatrix} -\frac{1}{\rho} & 0 & \frac{v_j}{\rho} \\ 0 & -\frac{1}{\rho} & \frac{v_k}{\rho} \\ \frac{v_j}{\rho} & \frac{v_k}{\rho} & -\frac{|v|^2}{\rho} \end{pmatrix} = -\frac{|v|^2}{\rho^3} + \frac{v_j^2}{\rho^3} + \frac{v_k^2}{\rho^3}, j, k = 1, \dots, d; j \neq k,$$

which is nonpositive. Finally, $l = 4$ gives

$$\mathcal{M}_4^3 = \det \begin{pmatrix} -\frac{1}{\rho} & 0 & 0 & \frac{v_1}{\rho} \\ 0 & -\frac{1}{\rho} & 0 & \frac{v_2}{\rho} \\ 0 & 0 & -\frac{1}{\rho} & \frac{v_3}{\rho} \\ \frac{v_1}{\rho} & \frac{v_2}{\rho} & \frac{v_3}{\rho} & -\frac{|v|^2}{\rho} \end{pmatrix} = \begin{pmatrix} - & R_1 & - \\ - & R_2 & - \\ - & R_3 & - \\ - & R_4 & - \end{pmatrix},$$

where $\{R_1, R_2, R_3, R_4\}$ denotes the rows. We observe that $R_4 = -v_1 R_1 - v_2 R_2 - v_3 R_3$; therefore, the rows are linearly dependent and $\mathcal{M}_4^3 = 0$. As such, the principal minors satisfy the nonpositive/nonnegative requirements for negative semidefiniteness of \mathcal{H} . \square

References

- [1] W.H. Reed, T. Hill, Triangular mesh methods for the neutron transport equation, Tech. Rep., Los Alamos Scientific Lab., N. Mex., USA, 1973.
- [2] F. Bassi, S. Rebay, High-order accurate discontinuous finite element solution of the 2D Euler equations, *J. Comput. Phys.* 138 (2) (1997) 251–285.
- [3] F. Bassi, S. Rebay, A high-order accurate discontinuous finite element method for the numerical solution of the compressible Navier–Stokes equations, *J. Comput. Phys.* 131 (2) (1997) 267–279.
- [4] B. Cockburn, C.-W. Shu, The Runge–Kutta discontinuous Galerkin method for conservation laws V: multidimensional systems, *J. Comput. Phys.* 141 (2) (1998) 199–224.
- [5] B. Cockburn, G. Karniadakis, C.-W. Shu, The development of discontinuous Galerkin methods, in: *Discontinuous Galerkin Methods*, Springer, 2000, pp. 3–50.
- [6] Z. Wang, K. Fidkowski, R. Abgrall, F. Bassi, D. Caraeni, A. Cary, H. Deconinck, R. Hartmann, K. Hillewaert, H. Huynh, N. Kroll, G. May, P.-O. Persson, B. van Leer, M. Visbal, High-order CFD methods: current status and perspective, *Int. J. Numer. Methods Fluids* (2013), <https://doi.org/10.1002/fld.3767>.
- [7] R. Abgrall, Generalisation of the Roe scheme for the computation of mixture of perfect gases, *Rech. Aérop.* 6 (1988) 31–43.
- [8] S. Karni, Multicomponent flow calculations by a consistent primitive algorithm, *J. Comput. Phys.* 112 (1) (1994) 31–43, <https://doi.org/10.1006/jcph.1994.1080>.
- [9] R. Abgrall, How to prevent pressure oscillations in multicomponent flow calculations: a quasi conservative approach, *J. Comput. Phys.* 125 (1) (1996) 150–160, <https://doi.org/10.1006/jcph.1996.0085>.
- [10] R. Abgrall, S. Karni, Computations of compressible multifluids, *J. Comput. Phys.* 169 (2) (2001) 594–623, <https://doi.org/10.1006/jcph.2000.6685>.
- [11] G. Billet, J. Ryan, A Runge–Kutta discontinuous Galerkin approach to solve reactive flows: the hyperbolic operator, *J. Comput. Phys.* 230 (4) (2011) 1064–1083, <https://doi.org/10.1016/j.jcp.2010.10.025>.
- [12] Y. Lv, M. Ihme, Discontinuous Galerkin method for multicomponent chemically reacting flows and combustion, *J. Comput. Phys.* 270 (2014) 105–137, <https://doi.org/10.1016/j.jcp.2014.03.029>.
- [13] K. Bando, M. Sekachev, M. Ihme, Comparison of algorithms for simulating multi-component reacting flows using high-order discontinuous Galerkin methods, <https://doi.org/10.2514/6.2020-1751>, 2020.
- [14] R.F. Johnson, A.D. Kercher, A conservative discontinuous Galerkin discretization for the chemically reacting Navier–Stokes equations, *J. Comput. Phys.* 423 (2020) 109826, <https://doi.org/10.1016/j.jcp.2020.109826>.
- [15] R. Deiterding, Parallel adaptive simulation of multi-dimensional detonation structures, Dissertation, 2003.
- [16] A. Gouasmi, K. Duraisamy, S.M. Murman, E. Tadmor, A minimum entropy principle in the compressible multicomponent Euler equations, *ESAIM: Math. Model. Numer. Anal.* 54 (2) (2020) 373–389.

- [17] Y. Lv, M. Ihme, Entropy-bounded discontinuous Galerkin scheme for Euler equations, *J. Comput. Phys.* 295 (2015) 715–739.
- [18] L. Friedrich, G. Schnücke, A.R. Winters, D.C.D.R. Fernández, G.J. Gassner, M.H. Carpenter, Entropy stable space–time discontinuous Galerkin schemes with summation-by-parts property for hyperbolic conservation laws, *J. Sci. Comput.* 80 (1) (2019) 175–222.
- [19] E.J. Ching, R.F. Johnson, A.D. Kercher, Positivity-preserving and entropy-bounded discontinuous Galerkin method for the chemically reacting, compressible Euler equations. Part II: the multidimensional case, arXiv preprint, arXiv:2211.16297, 2022.
- [20] X. Zhang, C.-W. Shu, On positivity-preserving high order discontinuous Galerkin schemes for compressible Euler equations on rectangular meshes, *J. Comput. Phys.* 229 (23) (2010) 8918–8934.
- [21] X. Zhang, Y. Xia, C.-W. Shu, Maximum-principle-satisfying and positivity-preserving high order discontinuous Galerkin schemes for conservation laws on triangular meshes, *J. Sci. Comput.* 50 (1) (2012) 29–62.
- [22] Y. Jiang, H. Liu, Invariant-region-preserving DG methods for multi-dimensional hyperbolic conservation law systems, with an application to compressible Euler equations, *J. Comput. Phys.* 373 (2018) 385–409.
- [23] P.-O. Persson, J. Peraire, Sub-cell shock capturing for discontinuous Galerkin methods, in: *AIAA (Ed.), 44th AIAA Aerospace Sciences Meeting and Exhibit, 2006, AIAA-2006-112*.
- [24] G. Barter, D. Darmofal, Shock capturing with PDE-based artificial viscosity for DGfem: part I. Formulation, *J. Comput. Phys.* 229 (5) (2010) 1810–1827.
- [25] E. Ching, Y. Lv, P. Gnoffo, M. Barnhardt, M. Ihme, Shock capturing for discontinuous Galerkin methods with application to predicting heat transfer in hypersonic flows, *J. Comput. Phys.* 376 (2019) 54–75.
- [26] H. Luo, J. Baum, R. Löhrner, A Hermite weno-based limiter for discontinuous Galerkin method on unstructured grids, *J. Comput. Phys.* 225 (1) (2007) 686–713.
- [27] A. Mazaheri, C.-W. Shu, V. Perrier, Bounded and compact weighted essentially nonoscillatory limiters for discontinuous Galerkin schemes: triangular elements, *J. Comput. Phys.* 395 (2019) 461–488.
- [28] B. Cockburn, C.-W. Shu, TVB Runge-Kutta local projection discontinuous Galerkin finite element method for conservation laws. II. General framework, *Math. Comput.* 52 (186) (1989) 411–435.
- [29] B. Cockburn, S.-Y. Lin, C.-W. Shu, TVB Runge-Kutta local projection discontinuous Galerkin finite element method for conservation laws III: one-dimensional systems, *J. Comput. Phys.* 84 (1) (1989) 90–113.
- [30] L. Krivodonova, Limiters for high-order discontinuous Galerkin methods, *J. Comput. Phys.* 226 (1) (2007) 879–896.
- [31] A. Corrigan, A. Kercher, D. Kessler, A moving discontinuous Galerkin finite element method for flows with interfaces, *Int. J. Numer. Methods Fluids* 89 (9) (2019) 362–406, <https://doi.org/10.1002/fld.4697>.
- [32] M. Zahr, P.-O. Persson, An optimization-based approach for high-order accurate discretization of conservation laws with discontinuous solutions, *J. Comput. Phys.* (2018).
- [33] M.J. Zahr, J.M. Powers, High-order resolution of multidimensional compressible reactive flow using implicit shock tracking, *AIAA J.* 59 (1) (2021) 150–164.
- [34] X. Zhang, C.-W. Shu, Positivity-preserving high order discontinuous Galerkin schemes for compressible Euler equations with source terms, *J. Comput. Phys.* 230 (4) (2011) 1238–1248.
- [35] X. Zhang, On positivity-preserving high order discontinuous Galerkin schemes for compressible Navier–Stokes equations, *J. Comput. Phys.* 328 (2017) 301–343.
- [36] X. Zhang, C.-W. Shu, A minimum entropy principle of high order schemes for gas dynamics equations, *Numer. Math.* 121 (3) (2012) 545–563.
- [37] Y. Lv, M. Ihme, High-order discontinuous Galerkin method for applications to multicomponent and chemically reacting flows, *Acta Mech. Sin.* 33 (3) (2017) 486–499.
- [38] K. Wu, C.-W. Shu, Geometric quasilinearization framework for analysis and design of bound-preserving schemes, arXiv preprint, arXiv:2111.04722, <https://arxiv.org/abs/2111.04722>, 2021.
- [39] J.-L. Guermond, B. Popov, I. Tomas, Invariant domain preserving discretization-independent schemes and convex limiting for hyperbolic systems, *Comput. Methods Appl. Mech. Eng.* 347 (2019) 143–175.
- [40] W. Pazner, Sparse invariant domain preserving discontinuous Galerkin methods with subcell convex limiting, *Comput. Methods Appl. Mech. Eng.* 382 (2021) 113876.
- [41] J. Gutiérrez-Jorquera, F. Kummer, A fully coupled high-order discontinuous Galerkin method for diffusion flames in a low-Mach number framework, *Int. J. Numer. Methods Fluids* (2022).
- [42] G. May, K. Devesse, A. Rangarajan, T. Magin, A hybridized discontinuous Galerkin solver for high-speed compressible flow, *Aerospace* 8 (11) (2021) 322.
- [43] A. Papoutsakis, S.S. Sazhin, S. Begg, I. Danaila, F. Luddens, An efficient Adaptive Mesh Refinement (AMR) algorithm for the discontinuous Galerkin method: applications for the computation of compressible two-phase flows, *J. Comput. Phys.* 363 (2018) 399–427.
- [44] C. Wang, X. Zhang, C.-W. Shu, J. Ning, Robust high order discontinuous Galerkin schemes for two-dimensional gaseous detonations, *J. Comput. Phys.* 231 (2) (2012) 653–665.
- [45] J. Du, Y. Yang, Third-order conservative sign-preserving and steady-state-preserving time integrations and applications in stiff multispecies and multireaction detonations, *J. Comput. Phys.* 395 (2019) 489–510.
- [46] J. Du, C. Wang, C. Qian, Y. Yang, High-order bound-preserving discontinuous Galerkin methods for stiff multispecies detonation, *SIAM J. Sci. Comput.* 41 (2) (2019) B250–B273.
- [47] J. Huang, C.-W. Shu, Bound-preserving modified exponential Runge–Kutta discontinuous Galerkin methods for scalar hyperbolic equations with stiff source terms, *J. Comput. Phys.* 361 (2018) 111–135.
- [48] J. Huang, C.-W. Shu, Positivity-preserving time discretizations for production–destruction equations with applications to non-equilibrium flows, *J. Sci. Comput.* 78 (3) (2019) 1811–1839.
- [49] J. Huang, W. Zhao, C.-W. Shu, A third-order unconditionally positivity-preserving scheme for production–destruction equations with applications to non-equilibrium flows, *J. Sci. Comput.* 79 (2) (2019) 1015–1056.
- [50] J. Pan, Y.-Y. Chen, L.-S. Fan, Second-order unconditional positive preserving schemes for non-equilibrium reactive flows with mass and mole balance, *J. Comput. Phys.* (2021) 110477.
- [51] A. Gouasmi, K. Duraisamy, S.M. Murman, Formulation of entropy-stable schemes for the multicomponent compressible Euler equations, *Comput. Methods Appl. Mech. Eng.* 363 (2020) 112912.
- [52] F. Renac, Entropy stable, robust and high-order DGSEM for the compressible multicomponent Euler equations, *J. Comput. Phys.* 445 (2021) 110584.
- [53] A. Peyvan, K. Shukla, J. Chan, G. Karniadakis, High-order methods for hypersonic flows with strong shocks and real chemistry, arXiv preprint, arXiv:2211.12635, 2022.
- [54] T. Chen, C.-W. Shu, Entropy stable high order discontinuous Galerkin methods with suitable quadrature rules for hyperbolic conservation laws, *J. Comput. Phys.* 345 (2017) 427–461.
- [55] J. Chan, L.C. Wilcox, On discretely entropy stable weight-adjusted discontinuous Galerkin methods: curvilinear meshes, *J. Comput. Phys.* 378 (2019) 366–393.
- [56] J. Chan, On discretely entropy conservative and entropy stable discontinuous Galerkin methods, *J. Comput. Phys.* 362 (2018) 346–374.
- [57] J. Crean, J.E. Hicken, D.C.D.R. Fernández, D.W. Zingg, M.H. Carpenter, Entropy-stable summation-by-parts discretization of the Euler equations on general curved elements, *J. Comput. Phys.* 356 (2018) 410–438.
- [58] T. Chen, C.-W. Shu, Review of entropy stable discontinuous Galerkin methods for systems of conservation laws on unstructured simplex meshes, *CSIAM Trans. Appl. Math.* 1 (1) (2020) 1–52.
- [59] G.J. Gassner, A.R. Winters, A novel robust strategy for discontinuous Galerkin methods in computational fluid mechanics: why? When? What? Where?, *Front. Phys.* (2021) 612.

- [60] V. Giovangigli, Multicomponent Flow Modeling, Birkhauser, Boston, 1999.
- [61] B.J. McBride, S. Gordon, M.A. Reno, Coefficients for calculating thermodynamic and transport properties of individual species, 1993.
- [62] B.J. McBride, M.J. Zehe, S. Gordon, NASA Glenn coefficients for calculating thermodynamic properties of individual species, 2002.
- [63] R.J. Kee, F.M. Rupley, E. Meeks, J.A. Miller, CHEMKIN-III: a FORTRAN chemical kinetics package for the analysis of gas-phase chemical and plasma kinetics, Tech. Rep., Sandia National Labs, Livermore, CA, United States, 1996.
- [64] F.A. Lindemann, S. Arrhenius, I. Langmuir, N. Dhar, J. Perrin, W.M. Lewis, Discussion on “the radiation theory of chemical action”, Trans. Faraday Soc. 17 (1922) 598–606.
- [65] R. Gilbert, K. Luther, J. Troe, Theory of thermal unimolecular reactions in the fall-off range. II. Weak collision rate constants, Ber. Bunsenges. Phys. Chem. 87 (2) (1983) 169–177.
- [66] R. Hartmann, T. Leicht, Higher order and adaptive DG methods for compressible flows, in: H. Deconinck (Ed.), VKI LS 2014-03: 37th Advanced VKI CFD Lecture Series: Recent Developments in Higher Order Methods and Industrial Application in Aeronautics, Dec. 9–12, 2013, Von Karman Institute for Fluid Dynamics, Rhode Saint Genèse, Belgium, 2014.
- [67] G. Strang, On the construction and comparison of difference schemes, SIAM J. Numer. Anal. 5 (3) (1968) 506–517.
- [68] N. Tsuboi, S. Katoh, A.K. Hayashi, Three-dimensional numerical simulation for hydrogen/air detonation: rectangular and diagonal structures, Proc. Combust. Inst. 29 (2) (2002) 2783–2788.
- [69] J. Crane, J.T. Lipkowitz, X. Shi, I. Wloka, A.M. Kempf, H. Wang, Three-dimensional detonation structure and its response to confinement, Proc. Combust. Inst. 39 (3) (2023) 2915–2923.
- [70] P.C. Ma, H. Wu, J.W. Labahn, T. Jaravel, M. Ihme, Analysis of transient blow-out dynamics in a swirl-stabilized combustor using large-eddy simulations, Proc. Combust. Inst. 37 (4) (2019) 5073–5082.
- [71] R. Bielawski, S. Barwey, S. Prakash, V. Raman, Highly-scalable GPU-accelerated compressible reacting flow solver for modeling high-speed flows, Comput. Fluids (2023) 105972.
- [72] H. Peng, R. Deiterding, A three-dimensional solver for simulating detonation on curvilinear adaptive meshes, Comput. Phys. Commun. 288 (2023) 108752.
- [73] S. Yang, S. Nagaraja, W. Sun, V. Yang, Multiscale modeling and general theory of non-equilibrium plasma-assisted ignition and combustion, J. Phys. D, Appl. Phys. 50 (43) (2017) 433001.
- [74] H. Wu, P.C. Ma, M. Ihme, Efficient time-stepping techniques for simulating turbulent reactive flows with stiff chemistry, Comput. Phys. Commun. 243 (2019) 81–96.
- [75] S. Blanes, F. Casas, P. Chartier, A. Murua, Optimized high-order splitting methods for some classes of parabolic equations, Math. Comput. 82 (283) (2013) 1559–1576.
- [76] H. Atkins, C. Shu, Quadrature-free implementation of discontinuous Galerkin methods for hyperbolic equations, ICASE Report 96-51, 1996, Tech. Rep., NASA Langley Research Center, August 1996, nASA-CR-201594.
- [77] H.L. Atkins, C.-W. Shu, Quadrature-free implementation of discontinuous Galerkin method for hyperbolic equations, AIAA J. 36 (5) (1998) 775–782.
- [78] A. Harten, P.D. Lax, B.V. Leer, On upstream differencing and Godunov-type schemes for hyperbolic conservation laws, SIAM Rev. 25 (1) (1983) 35–61.
- [79] M.S. Mock, Systems of conservation laws of mixed type, J. Differ. Equ. 37 (1) (1980) 70–88.
- [80] E. Tadmor, A minimum entropy principle in the gas dynamics equations, Appl. Numer. Math. 2 (3–5) (1986) 211–219.
- [81] E. Tadmor, Skew-selfadjoint form for systems of conservation laws, J. Math. Anal. Appl. 103 (2) (1984) 428–442.
- [82] C. Chalons, F. Coquel, E. Godlewski, P.-A. Raviart, N. Seguin, Godunov-type schemes for hyperbolic systems with parameter-dependent source: the case of Euler system with friction, Math. Models Methods Appl. Sci. 20 (11) (2010) 2109–2166.
- [83] F. Bouchut, Nonlinear Stability of Finite Volume Methods for Hyperbolic Conservation Laws: And Well-Balanced Schemes for Sources, Springer Science & Business Media, 2004.
- [84] T. Ruggeri, Galilean invariance and entropy principle for systems of balance laws, Contin. Mech. Thermodyn. 1 (1) (1989) 3–20.
- [85] K. Wu, Minimum principle on specific entropy and high-order accurate invariant region preserving numerical methods for relativistic hydrodynamics, arXiv preprint, arXiv:2102.03801, 2021.
- [86] J.-L. Guermond, B. Popov, Invariant domains and first-order continuous finite element approximation for hyperbolic systems, SIAM J. Numer. Anal. 54 (4) (2016) 2466–2489.
- [87] B. Perthame, C.-W. Shu, On positivity preserving finite volume schemes for Euler equations, Numer. Math. 73 (1) (1996) 119–130.
- [88] P. Lax, Shock waves and entropy, in: Contributions to Nonlinear Functional Analysis, Elsevier, 1971, pp. 603–634.
- [89] E. Toro, Riemann Solvers and Numerical Methods for Fluid Dynamics: A Practical Introduction, Springer Science & Business Media, 2013.
- [90] S. Gottlieb, C. Shu, E. Tadmor, Strong stability-preserving high-order time discretization methods, SIAM Rev. 43 (1) (2001) 89–112.
- [91] R. Spiteri, S. Ruuth, A new class of optimal high-order strong-stability-preserving time discretization methods, SIAM J. Numer. Anal. 40 (2) (2002) 469–491.
- [92] J.-L. Guermond, B. Popov, Fast estimation from above of the maximum wave speed in the Riemann problem for the Euler equations, J. Comput. Phys. 321 (2016) 908–926.
- [93] E.F. Toro, L.O. Müller, A. Sivilgia, Bounds for wave speeds in the Riemann problem: direct theoretical estimates, Comput. Fluids 209 (2020) 104640.
- [94] R. Frolov, An efficient algorithm for the multicomponent compressible Navier–Stokes equations in low- and high-Mach number regimes, Comput. Fluids 178 (2019) 15–40.
- [95] B. Cockburn, C.-W. Shu, Runge–Kutta discontinuous Galerkin methods for convection-dominated problems, J. Sci. Comput. 16 (3) (2001) 173–261.
- [96] T. Dzanic, F.D. Witherden, Positivity-preserving entropy-based adaptive filtering for discontinuous spectral element methods, J. Comput. Phys. 468 (2022) 111501.
- [97] W. Trojak, T. Dzanic, Positivity-preserving discontinuous spectral element methods for compressible multi-species flows, arXiv preprint, arXiv:2308.02426, 2023.
- [98] E. Toro, V. Titarev, Solution of the generalized Riemann problem for advection–reaction equations, Proc. R. Soc. Lond., Ser. A, Math. Phys. Eng. Sci. 458 (2018) 271–281.
- [99] G. Montecinos, C.E. Castro, M. Dumbser, E.F. Toro, Comparison of solvers for the generalized Riemann problem for hyperbolic systems with source terms, J. Comput. Phys. 231 (19) (2012) 6472–6494.
- [100] A. Beccantini, Riemann solvers for multi-component gas mixtures with temperature dependent heat capacities, Ph.D. thesis, Université d’Évry Val-d’Essonne, 2000.
- [101] A. Beccantini, E. Studer, The reactive Riemann problem for thermally perfect gases at all combustion regimes, Int. J. Numer. Methods Fluids 64 (3) (2010) 269–313.
- [102] E. Hairer, G. Wanner, Solving Ordinary Differential Equations II. Stiff and Differential-Algebraic Problems, vol. 14, 1996.
- [103] L. Formaggia, A. Scotti, Positivity and conservation properties of some integration schemes for mass action kinetics, SIAM J. Numer. Anal. 49 (3) (2011) 1267–1288.
- [104] A. Sandu, Positive numerical integration methods for chemical kinetic systems, J. Comput. Phys. 170 (2) (2001) 589–602.
- [105] G.J. Gassner, A skew-symmetric discontinuous Galerkin spectral element discretization and its relation to SBP-SAT finite difference methods, SIAM J. Sci. Comput. 35 (3) (2013) A1233–A1253.
- [106] G.J. Gassner, A.R. Winters, D.A. Kopriva, Split form nodal discontinuous Galerkin schemes with summation-by-parts property for the compressible Euler equations, J. Comput. Phys. 327 (2016) 39–66.

- [107] P.L. Roe, Affordable, entropy consistent flux functions, in: Eleventh International Conference on Hyperbolic Problems: Theory, Numerics and Applications, Lyon, 2006.
- [108] F. Ismail, P.L. Roe, Affordable, entropy-consistent Euler flux functions II: entropy production at shocks, *J. Comput. Phys.* 228 (15) (2009) 5410–5436.
- [109] J.C. Slattery, P.G. Cizmas, A.N. Karpets, S.B. Chambers, Role of differential entropy inequality in chemically reacting flows, *Chem. Eng. Sci.* 66 (21) (2011) 5236–5243.
- [110] A.E. Ream, J.C. Slattery, P.G. Cizmas, A method for generating reduced-order combustion mechanisms that satisfy the differential entropy inequality, *Phys. Fluids* 30 (4) (2018) 043601.
- [111] A. Corrigan, A. Kercher, J. Liu, K. Kailasanath, Jet noise simulation using a higher-order discontinuous Galerkin method, in: 2018 AIAA SciTech Forum, 2018, AIAA-2018-1247.
- [112] K. Bando, Towards high-performance discontinuous Galerkin simulations of reacting flows using Legion, Ph.D. thesis, Stanford University, 2023.
- [113] R. Houim, K. Kuo, A low-dissipation and time-accurate method for compressible multi-component flow with variable specific heat ratios, *J. Comput. Phys.* 230 (23) (2011) 8527–8553, <https://doi.org/10.1016/j.jcp.2011.07.031>.
- [114] G.P. Smith, D.M. Golden, M. Frenklach, N.W. Moriarty, B. Eiteneer, M. Goldenberg, C.T. Bowman, Gri-mech 3.0, version 3.0, 2000.
- [115] J.E. Shepherd, Explosion dynamics laboratory: shock and detonation toolbox - 2018 version, JES 9-19-2018, <http://shepherd.caltech.edu/EDL/PublicResources/sdt/>, 2018.
- [116] M. Bolla, B. Bullins, S. Chaturapruek, S. Chen, K. Friedl, Spectral properties of modularity matrices, *Linear Algebra Appl.* 473 (2015) 359–376.
- [117] P. Dube, R. Jain, Bertrand games between multi-class queues, in: Proceedings of the 48th IEEE Conference on Decision and Control (CDC) Held Jointly with 2009 28th Chinese Control Conference, IEEE, 2009, pp. 8588–8593.